1995-09

South China Sea warm-core and cold-core eddies detected from the Navy's Master Oceanographic Observation Data Set (MOODS)

Tseng, Hsing-Chia

Monterey, California. Naval Postgraduate School

NAVAL POSTGRADUATE SCHOOL
MONTEREY, CALIFORNIA

THESIS

SOUTH CHINA SEA WARM-CORE AND COLD-CORE EDDIES DETECTED FROM THE NAVY'S MASTER OCEANOGRAPHIC OBSERVATION DATA SET (MOODS)

by

Tseng, Hsing-Chia

September, 1995

Thesis Advisor: Peter C. Chu
Co-Advisor: C. P. Chang

Approved for public release; distribution is unlimited.

REPORT DOCUMENTATION PAGE

Form Approved OMB No. 0704-0188

1. AGENCY USE ONLY *(Leave blank)*	2. REPORT DATE	3. REPORT TYPE AND DATES COVERED
	September 1995	Master's Thesis

4. TITLE AND SUBTITLE TITLE OF THESIS **SOUTH CHINA SEA WARM-CORE AND COLD-CORE EDDIES DETECTED FROM THE NAVY'S MASTER OCEANOGRAPHIC OBSERVATION DATA SET (MOODS)**

5. FUNDING NUMBERS

6. AUTHOR(S) Tseng, Hsing-Chia

7. PERFORMING ORGANIZATION NAME(S) AND ADDRESS(ES)
Naval Postgraduate School
Monterey CA 93943-5000

8. PERFORMING ORGANIZATION REPORT NUMBER

9. SPONSORING/MONITORING AGENCY NAME(S) AND ADDRESS(ES)

10. SPONSORING/MONITORING AGENCY REPORT NUMBER

11. SUPPLEMENTARY NOTES The views expressed in this thesis are those of the author and do not reflect the official policy or position of the Department of Defense or the U.S. Government.

12a. DISTRIBUTION/AVAILABILITY STATEMENT
Approved for public release; distribution is unlimited.

12b. DISTRIBUTION CODE

13. ABSTRACT *(maximum 200 words)* A South China Sea warm-core eddy with sea surface temperatures (SST) higher than 29.5°C, recently reported by Chu and Chang (1995), appears in the central South China Sea (west of Luzon Island) in boreal spring, and strengthens until the onset of the summer monsoon (mid-May), then weakens and disappears at the end of May. Although its size and intensity varies, the warm-core eddy releases large moisture and heat fluxes into the atmosphere and in turn affects the monsoon circulation. The transient features and interannual variabilities of the warm-core eddy have not yet been studied. In this study we use 189,059 temperature profiles from the U.S. Navy's Master Oceanographic Observation Data Set (MOODS) to investigate the eddy features. We use Optimal Interpolation to create a ten-day interval synoptic data set for 1964-84 on a 0.5°x 1° grid (finer resolution in zonal direction) from the MOODS SST data. Then, we formulate an Emprical Orthogonal Functions (EOF) analysis. The first EOF mode accounts for 35.5% of the variance and is characterized by a field which is similar to the mean field. The second EOF mode accounts for 21.4% of the variance and is characterized by a meso-scale eddy (116°-119°E, 16°-19°N) to the west of Luzon Island. The size of the eddy is around 100,000 km^2. The time series of EOF2 behave differently between El Niño and non-El Niño years: a warm-core eddy often appears during the non-El Niño years, and a cold-core eddy usually exists during the El Niño years. A new scenario of the air-sea feedback is proposed for the warm-core eddy formation in non-El Niño years and the cold-core eddy formation in El Niño years. A numerical simulation from a three dimensional primitive equation model shows the formation of a warm-core eddy under climatological forcing (more likely for the non-El Niño condition).

14. SUBJECT TERMS Warm-Core Eddy, Cold-Core Eddy, Variance, Cold Surge, Eigenvalues, Eigenvector, Covariance, Time Series, El Niño, EOF, Composite, Upwelling, Downwelling, Ekman Pumping Velocity

15. NUMBER OF PAGES 89

16. PRICE CODE

17. SECURITY CLASSIFICATION OF REPORT	18. SECURITY CLASSIFICATION OF THIS PAGE	19. SECURITY CLASSIFICATION OF ABSTRACT	20. LIMITATION OF ABSTRACT
Unclassified	Unclassified	Unclassified	UL

NSN 7540-01-280-5500

Standard Form 298 (Rev. 2-89)
Prescribed by ANSI Std. 239-18 298-102

Approved for public release; distribution is unlimited.

SOUTH CHINA SEA WARM-CORE AND COLD-CORE EDDIES DETECTED FROM THE NAVY'S MASTER OCEANOGRAPHIC OBSERVATION DATA SET (MOODS)

Tseng, Hsing-Chia
Lieutenant Commander, Republic of China Navy
B.S. Republic of China Naval Academy - 1982

Submitted in partial fulfillment
of the requirements for the degree of

MASTER OF SCIENCE
IN
PHYSICAL OCEANOGRAPHY
from the
NAVAL POSTGRADUATE SCHOOL
September 1995

Author: [redacted]
Tseng, Hsing-Chia

Approved by: [redacted]
Peter C. Chu, Thesis Advisor

[redacted]
C. P. Chang, Co-Advisor

[redacted]
Robert H. Bourke, Chairman
Department of Oceanography

ABSTRACT

A South China Sea warm-core eddy with sea surface temperatures (SST) higher than 29.5°C, recently reported by Chu and Chang (1995), appears in the central South China Sea (west of Luzon Island) in boreal spring, and strengthens until the onset of the summer monsoon (mid-May), then weakens and disappears at the end of May. Although its size and intensity varies, the warm-core eddy releases large moisture and heat fluxes into the atmosphere and in turn affects the monsoon circulation. The transient features and interannual variabilities of the warm-core eddy have not yet been studied. In this study we use 189,059 temperature profiles from the U.S. Navy's Master Oceanographic Observation Data Set (MOODS) to investigate the eddy features. We use Optimal Interpolation to create a ten-day interval synoptic data set for 1964-84 on a 0.5°x 1° grid (finer resolution in zonal direction) from the MOODS SST data. Then, we formulate an Emprical Orthogonal Functions (EOF) analysis. The first EOF mode accounts for 35.5% of the variance and is characterized by a field which is similar to the mean field. The second EOF mode accounts for 21.4% of the variance and is characterized by a meso-scale eddy (116°-119°E, 16°-19°N) to the west of Luzon Island. The size of the eddy is around 100,000 km^2. The time series of EOF2 behave differently between El Niño and non-El Niño years: a warm-core eddy often appears during the non-El Niño years, and a cold-core eddy usually exists during the El Niño years. A new scenario of the air-sea feedback is proposed for the warm-core eddy formation in non-El Niño years and the cold-core eddy formation in El Niño years. A numerical simulation from a three dimensional primitive equation model shows the formation of a warm-core eddy under climatological forcing (more likely for the non-El Niño condition).

TABLE OF CONTENTS

LIST OF FIGURES

LIST OF TABLES

ACKNOWLEDGEMENTS

The author is grateful to Jeng-Ming Chen for invaluable comments and to Ming-Jer Huang and Bao-Fong Jeng for programming assistance. Special thanks to Dr. Peter Chu for his guidance, patience and good humor. He made my work fun and challenging. Dr. Chang shared his wealth of meteorology knowledge with me and gave me many suggestions. This work was funded by the Naval Oceanographic Office, the Office of Naval Research NOMP Program, and the Naval Postgraduate School.

I. INTRODUCTION

The South China Sea (SCS) has a bottom topography (Figure 1) that makes it a unique semi-enclosed ocean basin that is overlaid by a pronounced monsoon surface wind. Extensive continental shelves (less than 100 m deep) are found on the western and southern parts, while steep slopes with almost no shelves are found in the eastern part of SCS. The deepest water is confined to a bowl-type trench. The maximum depth is around 5,000 m.

Based on limited data sets, studies show that eddies in the SCS are predominantly cyclonic in winter and spring and anti-cyclonic in summer, with sizes ranging from small to meso-scale (Huang et al., 1994). Both cold and warm eddies exist in the SCS. Dale (1956) and Uda and Nakao (1974) reported a cold eddy off the central Vietnamese Coast in summer. Nitan (1970) found a cold eddy located to the northwest of Luzon. Reports from the South China Sea Institute of Oceanology (SCSIO, 1985) indicate that in the central SCS, a warm-core eddy appears in summer and winter, but more closer to Vietnam in summer at the surface.

During boreal spring, the surface atmospheric circulation pattern changes from the pattern of the northern winter monsoon to that of the northern summer monsoon. In winter, a semi-permanent surface subtropical high pressure center prevails over the northwestern Pacific with its east-west axis located north of 20°N (Figure 2a). Cold surges tend to move directly from southeastern China to the SCS with north-northeasterly winds. The winter cold surges tend to enhance the atmospheric convective activity in the Malaysia-South China Sea Region (Cheang, 1980).

During spring, the surface atmospheric subtropical high pressure center moves closer to the equatorial region, with its east-west axis between 15°N and 20°N over the northern region of the SCS and northern Indochina Peninsula (Figure 2b). Cold surges do not move directly out from southeastern China. They travel a long distance across South Korea and southern Japan and around the subtropical high in the western Pacific. They

arrive in the southern region of the SCS as northeasterlies. Such a semi-permanent atmospheric surface anticyclone results in downwelling in the upper ocean.

Recently Chu and Chang (1995) reported a warm pool (SCSWP) in the central SCS (west of Luzon Island) during the late spring season, that strengthens until the onset of the summer monsoon (mid-May), then weakens and disappears at the end of May. Although its size and intensity varies, the SCSWP releases large moisture and heat fluxes into the atmosphere and in turn affects the monsoon circulation.

The thermal feature of eddies (warm-core or cold-core) greatly impacts on the monsoon circulation. Therefore, it is very important to know what kind of eddies occupy the central SCS in winter and spring seasons. Can we identify these eddies from the most complete data set - the U.S. Navy's Master Observational Oceanographic Data Set (MOODS)? What are the major features of the eddies?

The data set that we have used is a subset of MOODS and includes 189,059 profiles binned for the desired area coverage. The data set covers the years 1929 through 1994 and comes from numerous instrument types including XBT's, CTD's and reversing thermometers. Our study field covers the area 5°S - 25°N and 105°E - 120°N. The data were binned for every ten days creating 756 consecutive temporal groups called "points". The Optimum Interpolation (OI) technology was applied to create a gridded data set and the GMT Software (Wessel and Smith, 1993) was used to plot SST contours.

After the gridded data set has been established, we divided our study into three parts. First, a composite analysis of the gridded SST data was done to obtain the ensemble mean SST field and the mean seasonal variation. The latter shows strong evidence of the existence of a warm pool in the central SCS before the summer monsoon onset (April and early May). Second, the transient features of the SST field were quantitatively investigated using the method of Emprical Orthogonal Function (EOF) analysis. An air-sea feedback hypothesis was proposed after the EOF analysis. Third, in order to investigate the mechanism of the SCS warm-core eddy formation during boreal winter and summer under climatological forcing and its possible effects on the summer

monsoon onset, a primitive equation model with second-order turbulence closure (Blumberg and Meller, 1987) was used.

This thesis is organized as follows: Chapter II depicts the data sources, including the U.S. Navy's Master Oceanographic Observation Data Set (MOODS) and its temporal and spatial distributions as well as the establishment of gridded data set. Chapter III describes seasonal and interannual variabilities. Chapter IV discusses numerical simulations.

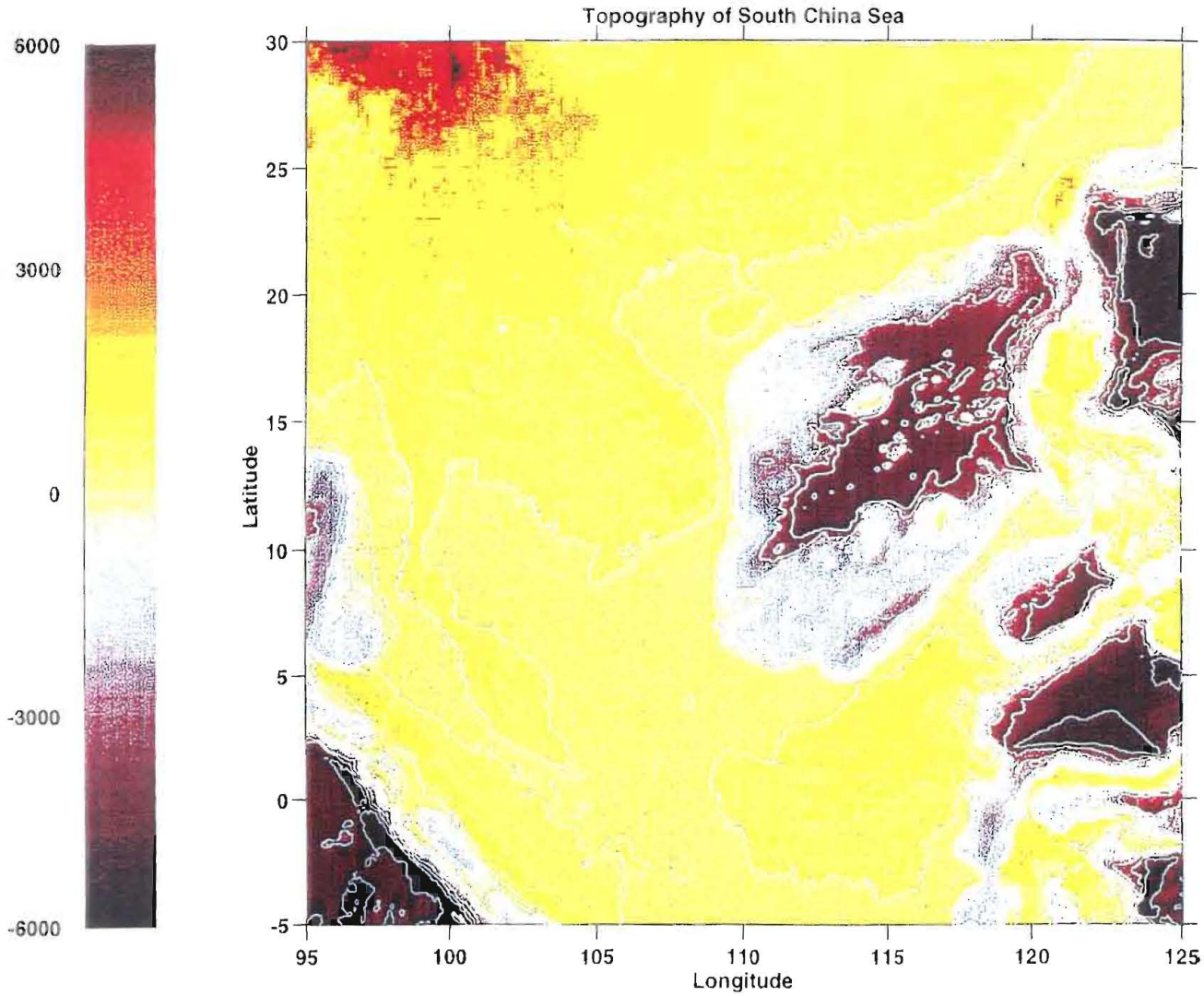

Figure 1. Geography and Isobaths in Meters, Showing the Bottom Topography of the South China Sea.

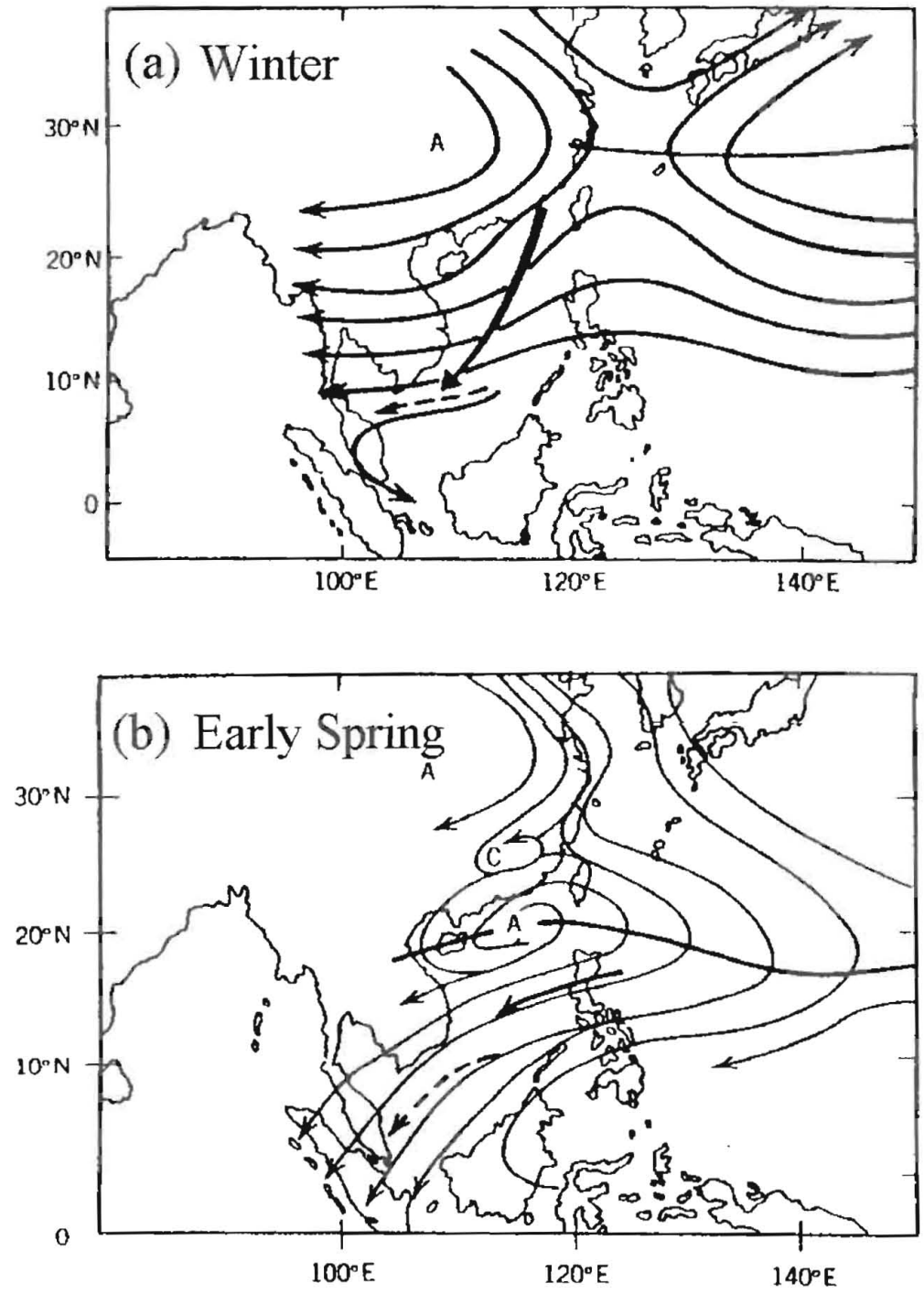

Figure 2. Mean Atmospheric Surface Streamline Analysis for (a) Winter, and (b) Early Spring (From Cheang, 1980).

II. DATA SOURCES

A. MASTER OCEANOGRAPHIC OBSERVATION DATA SET (MOODS)

The MOODS is a compilation of observed ocean data worldwide consisting of (a) temperature-only profiles; (b) both temperature and salinity profiles, (c) sound-speed profiles, and (d) surface temperature (drifting buoy). These measurements are, in general, irregular in time and space. In this study, we analyze temperature profiles obtained during 1964-84 from a variety of instruments. Due to the shear size (more than six million profiles) and enormous influx of data to NAVOCEANO from various sources, quality control is a difficult task. Our study domain includes the area 5°S to 25°N and 105° to 120°E; the data set within this region consisted of 189,059 temperature profiles after rejecting certain data during quality control. The primary editing procedures included removal of profiles with obviously erroneous location, profiles with large spikes, and profiles displaying features that do not match the characteristics of surrounding profiles. In shallow water, this procedure can be partially automated but also involves subjective interpretation because of the undersampling of MOODS compared to the spatial and temporal variability of the oceanography.

The temporal and spatial distribution of the MOODS data are irregular. The sparsity of profiles near the Sunda Shelf and western coastal region of Borneo is shown in Figure 3 and the temporal distribution from 1964 to 1984 is shown in Figure 4. Figure 4 indicates that most observations were obtained during the Vietnamese War (1965-69). There are nearly 14,800 profiles (maximum number of observations in a year) in 1968 (Figure 5). The minimum number of observations is in 1984 (near 3,000 profiles) (Figure 6). These figures indicate that the number of observations within a given year exhibits a seasonal variation.

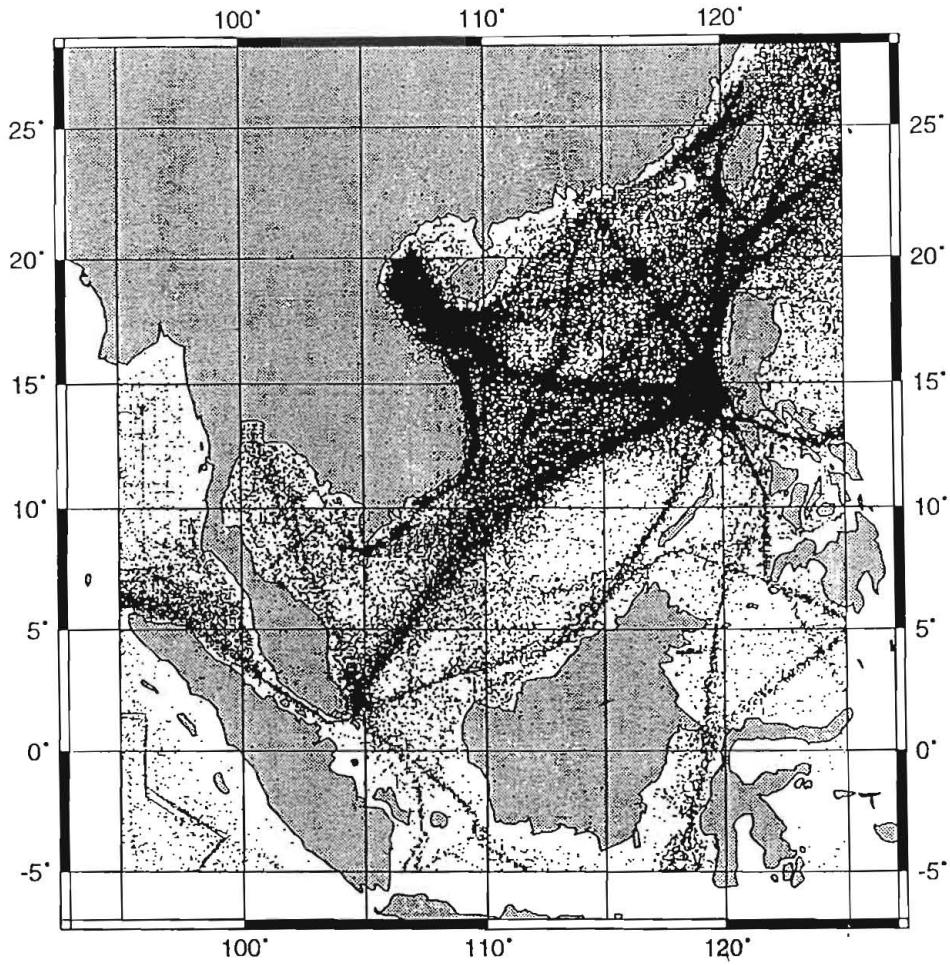

Figure 3. Spatial Distribution of MOODS Data during 1964-1984

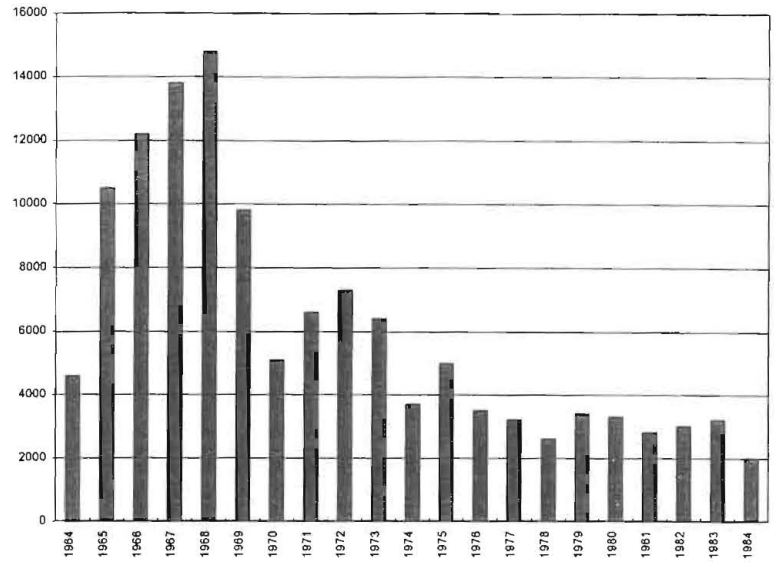

Figure 4. Temporal Distribution of MOODS Data during 1964-1984

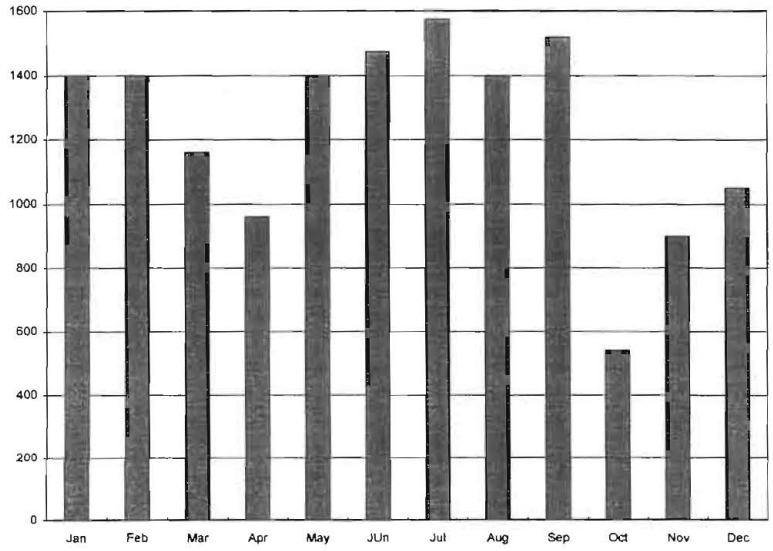

Figure 5. Temporal Distribution of MOODS Data for 1968

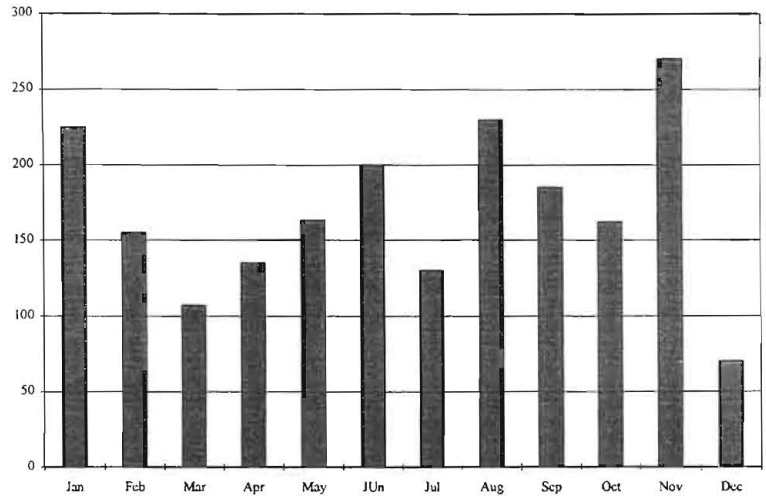

Figure 6. Temporal Distribution of MOODS Data for 1984

The main limitation of the MOODS data is its irregular distribution in time and space. Certain periods and areas are over sampled while others lack enough observations to gain any meaningful insight. Vertical resolution and data quality are also highly variable depending much on instrument type and sampling expertise. There are two data sparse area: the Sunda Shelf area and the western coastal region of Borneo (Figure 3). There are frequent ten to 20 day gaps of no observations in the whole South China Sea. Spatial and temporal irregularities along with the lack of data in certain regions must be carefully weighted in order to avoid statistically-induced variability.

B. ESTABLISHMENT OF GRIDDED DATA

Our near ten-day interval data set is distributed evenly in time and unevenly in space. We use the Optimum Interpolation scheme to obtain a gridded data set. We use the $1° \times 1°$ monthly SST climatology of Levitus (1982) as a mean field. For the same time period, the SST perturbations $T'_1, T'_2, \ldots, T'_N$ for SST observations were obtained by subtracting the climatological value at the closest grid point from the observation.

Optimum interpolation assigns a weight to each observation that accounts for variation in spatial sampling. The interpolated temperature anomaly at the grid point, T'_G, is a linear combination of the observed anomalies, $T'_1, T'_2, \ldots, T'_N$ with weights $\alpha_1, \alpha_2, \ldots, \alpha_N$.

$$T'_G = \sum_{i=1}^{N} \alpha_i T'_i \tag{1}$$

The values of the weights, $\alpha_i (i = 1,2,\ldots,N)$, are found by minimizing, in a least square sense, the difference between the interpolated value at the grid node and the true value there, and obtained from solving a set of N algebraic equations (Gardin, 1963)

$$\sum_{j=1}^{N} \alpha_j \mu_{ij} + \lambda^{-2} \alpha = \mu_{Gi} \tag{2}$$

where $i = 1,2,\ldots,N$. Here λ is the signal-to-noise ratio. μ_{ij} is the autocorrelation between locations i and j, and μ_{Gi} is the autocorrelation between the grid node and location i. Here, the autocorrelation function (ACF) is defined by

$$\mu = \frac{1}{s^2} \int^{R} T'(r_0) T'(r_0 + r) dr_0 \tag{3}$$

where r_0 denotes the independent space vector defining the location of points in a sampling space R, and r is the space lag and s^2 the variance. μ is computed by paring the anomalies into bins depending upon their separation in space, r. The values of μ are obtained from calculating the correlation coefficient for all the anomaly pairs in each bin. The ACF will be constructed for the combination of different lags and in the isotropic case

$$\eta(m) = \eta(0) \exp[-A^2 (m\Delta r)^2] \tag{4}$$

where $\eta(m)$ denotes the ACF value in the bin with the horizontal separation $m\Delta r$. Δr = 10 km is the increment for the space separation. A^{-1} is the horizontal decorrelation scales. Therefore, the autocorrelations μ_{ij} and μ_{Gi} are given by

$$\mu_{ij} = \eta(m_{ij}), \quad \mu_{Gi} = \eta(m_{Gi}) \tag{5}$$

where m_{ij} and m_{Gi} represent spatial separations between locations i and j, and between location i and the grid node.

The measured variance s^2 of the thermal fields is separated into signal and noise whereby

$$s^2 = s_s^2 + s_n^s \tag{6}$$

The noise variance is brought on from two sources, geophysical and instrumentation errors. The geophysical error is unresolved thermal variability with scales smaller than the typical time and space scales between two temperature profiles, and the instrumentation error is negligible compared to the geophysical error (White and Bernstein, 1979). In calculating the ACF value of the first bin (zero to 10 km lag) the temperature anomalies were never paired with themselves. The ACF value at the zero lag $\eta(0)$ was extrapolated from the first bin into the origin, and therefore does not equal 1. The signal-to-noise ratio is computed by (Sprintall and Meyers, 1991).

$$\lambda \equiv \frac{s_s}{s_n} = \sqrt{\frac{\eta(0)}{1-\eta(0)}} \tag{7}$$

The larger the λ, the less geophysical error exists. If $\eta(0) = 1$, there is no noise, $\lambda = \infty$; and if $\eta(0) = 0$, there is no signal, then $\lambda = 0$. If $\lambda > 2$, the ratio of the signal variance, s_s^2, to the noise variance, s_n^2, is greater than 4, which was considered a quite good condition by White et al. (1982) and Sprintall and Meyers (1991).

For each grid node location, (1) results in a set of N linear algebraic equations to be solved for N unknowns, α_i, by matrix inversion. In (1) the autocorrelations μ_{ij}, μ_{Gi},

and the signal-to-noise ratio λ have been computed at the surface from the MOODS data set. Therefore, the N weights α_i can be determined by solving (1), and thus any new observations $T_1', T_2', \ldots, T_N'$, can be interpolated into any grid node G.

We applied Optimal Interpolation to build up a 10-day interval synoptic data set for 1964-84 on a $0.5° \times 1°$ grids (finer resolution in zonal direction) from the MOODS temperature data. Our gridded data set consists of 756 consecutive SST fields from 1-10 January 1964 to 21-31 December 1984. An example of SST contours in 1980 is shown in Figure 7.

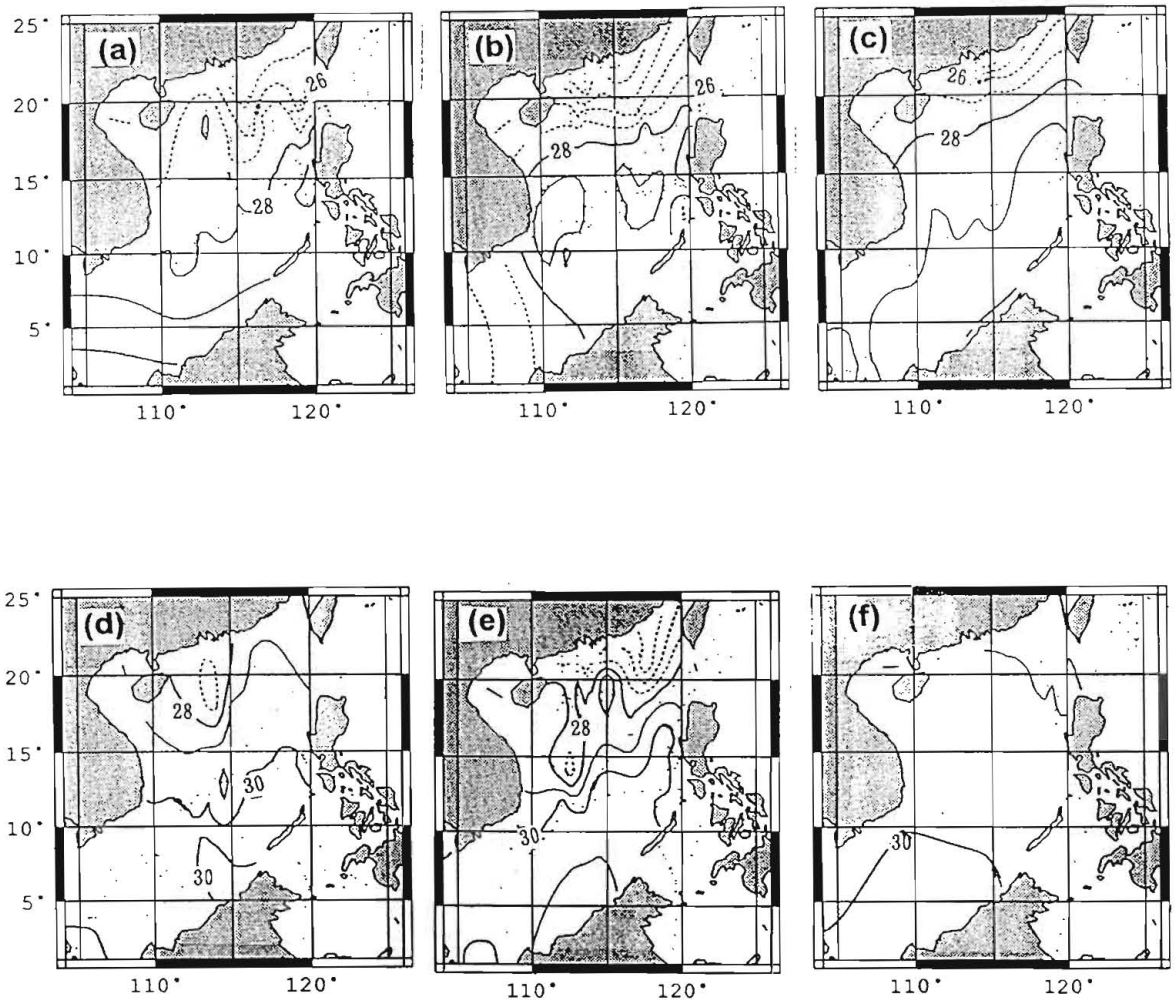

Figure 7. Consecutive SST Contours after the Establishment of Gridded Data in 1980: (a) April 1-10, (b) April 11-20, (c) April 21-30, (d) May 1-10, (e) May 11-20, (f) May 21-31. The Solid (Dash) Lines Means SST Higher (Lower) than 28°C. The Dots Indicate the MOODS Stations.

III. SEASONAL AND INTERANNUAL VARIABILITIES

A. SCS WARM-CORE EDDY CASE STUDIES

Chu and Chang (1995) reported a warm-core eddy (SST ≥29°C) appears in the central SCS before the summer monsoon onset from analyzing the MOODS data for 1966. A warm-core eddy often appears in spring and disappears in later May. The SST field in 1966 shows the following features:

1. Flat SST Pattern in March

This period is right after the cessation of the northern winter monsoon but some hint of the winter monsoon characteristics are still present (Figure 8a-c). Surface isotherms in March show a pattern of northeast-southwest oriented isotherms with a positive temperature gradient towards the southeast near the equator. The warmest water (>29°C) appears off the northwest coast of Borneo. SST decreases from 29°C near the Borneo coast to 24° at the southeast coast of China.

2. Early Stage of Warm-Core Eddy

This period is in the center of the transition season (Figure 8d). In early April, a warm pool with the size of near 500,000 km^2 appears near the west coast of Luzon. The temperature of the warm water increases from 28°C (Figure 8d and e) to 30°C (Figure 8f).

3. Fully Developed Stage of SCS Warm-Core Eddy

This period occurs in late spring before the summer monsoon in the SCS begins (Figure 8g). The warm water pool expands southwestward. During May 1-10, the central SCS was dominated by warm water (>30°C). A warm pool with SST higher than 30.5°C is located at 111°-116°E, 7°-12°N. This warm pool provides a surface heating source for the formation of the atmospheric low pressure center, which will contribute to the summer (southwest) monsoon onset.

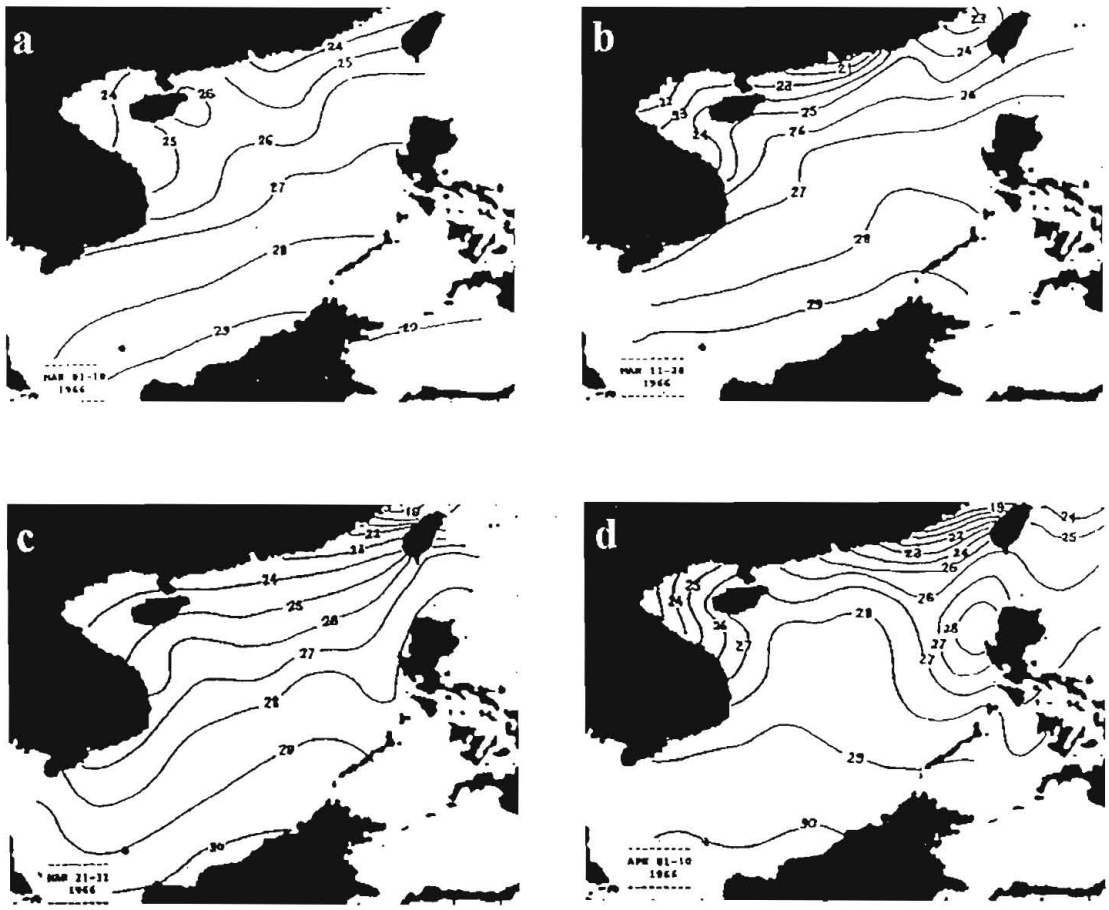

Figure 8. South China Sea SST Evolution in 1966: (a) March 1-10, (b) March 11-20, (c) March 21-31, (d) April 1-10 (From Chu and Chang, 1995).

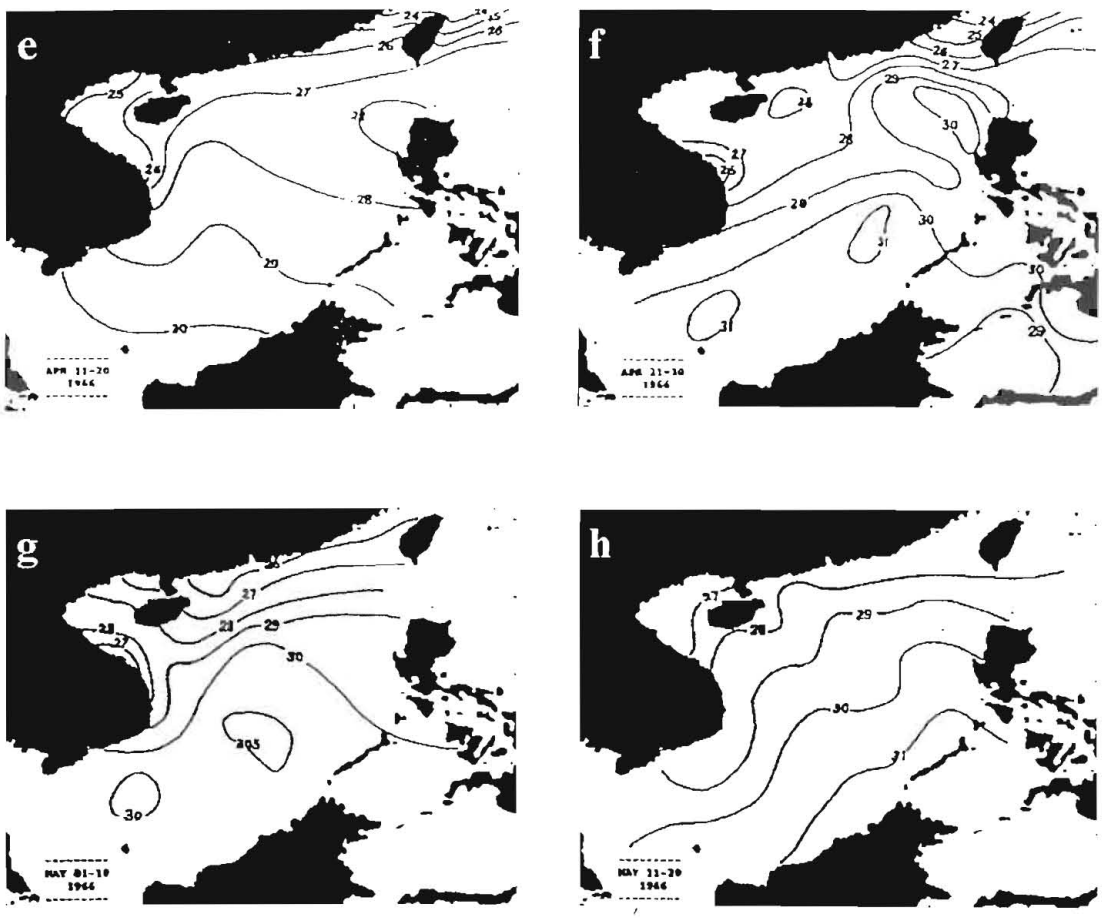

Figure 8. South China Sea SST Evolution in 1966: (e) April 11-20, (f) April 21-30, (g) May 1-10, (h) May 11-20 (From Chu and Chang, 1995).

4. Disappearing Stage of SCS Warm-Core Eddy

This period is just after the summer monsoon onset (Figure 8h). The SST for May 11-20 is relaxed back to the ensemble mean pattern and the SCSWP disappears. Warm water (>31 °C) appears off the northwest coast of Borneo and decreases from Borneo to the southeast coast of China.

5. Cold-Core Eddy Building-up by Coastal Upwelling

Under the steady summer (southwest) monsoon forcing, cold water will be upwelled near the southeast coast of China and Vietnam. A cold-core eddy appears off the southeast China coast (<25 °C) and off the Vietnamese coast (<28 °C).

B. COMPOSITE ANALYSIS

The existence of the central SCS warm-core eddy is likely to be important for the air-sea heat and moisture exchanges and its effects on the summer monsoon onset. The warm-core eddy was reported to the west of Luzon Island during the winter-to-summer monsoon transition in 1966 (Chu and Chang, 1995). We now examine the data to see if we can obtain a warm-core eddy signal from historical data. To answer this question, we need to perform a composite analysis. After the gridded data is established, the SST data are represented by $T(x_i, y_j, \tau_k, t_l)$, where (x_i, y_j) are the horizontal grids, τ_k = 1964, 1965,... 1984, is the time sequence in years, and t_l =1, 2, ... 36, the time sequence in ten day intervals. Before investigating the annual variation of SST, we define the following two temporal averages:

$$\overline{T}(x_i, y_j, t_l) \equiv \frac{1}{\Delta\tau} \sum_k T(x_i, y_j, \tau_k, t_l), \quad \Delta\tau \equiv 1984 - 1964 = 21 \text{ years} \tag{8}$$

which is the annual mean value, and

$$\overline{\overline{T}}(x_i, y_j) \equiv \frac{1}{36} \sum_{l=1}^{36} \overline{T}(x_i, y_j, t_l), \tag{9}$$

which is the ensemble mean value. The ensemble mean (1964-1984) SST field over the SCS (Figure 9) shows the pattern of northeast-southwest oriented isotherms with a

positive temperature gradient towards the southeast near the equator. The ensemble mean has a rather weak horizontal temperature gradient. $\overline{\overline{T}}$ decreases from 29°C near the Borneo coast to 26°C near the southeast China coast.

The annual mean value relative to the ensemble mean, $\widetilde{T}(x_i, y_j, t_l) = \overline{T}(x_i, y_j, t_l) - \overline{\overline{T}}(x_i, y_j)$, shows the composite features of the annual mean SST anomalies (Figure 10). The annual mean SST anomaly ($\widetilde{T}$) has the following features:

1. Cooling Phase

In March, $\widetilde{T}$ is negative almost everywhere throughout the whole SCS, and decreases from the west coast of Borneo to the southeast coast of China (Figure 10a-c). This indicates that the SCS is cooling during the winter and early spring seasons and that the rate of cooling is weakest near the Borneo coast and strongest near the Taiwan Strait (<-3°C).

2. Early Warming Phase

In early April (Figure 10d), positive $\widetilde{T}$ were found to the west of Luzon Island and the west coast of Borneo. At the Luzon Strait $\widetilde{T}$ is always negative until late April (21-30 April). This means that the early SCS warming starts in the central SCS by some local effects (e.g., a warm eddy but not by the Kuroshio intrusion!) and at the south SCS. It also implies that the Kuroshio water entering the SCS in April might be cooler than the SCS water (at least at the surface).

3. Central SCS Warming Phase

In May (Figure 10g-h), the central SCS warm-core eddy becomes stronger than the early warming phase. During 11-20 May (Figure 10h), the central SCS warm-core eddy ($\widetilde{T} > 1.8$°C) accounts for the maximum annual mean warm anomaly.

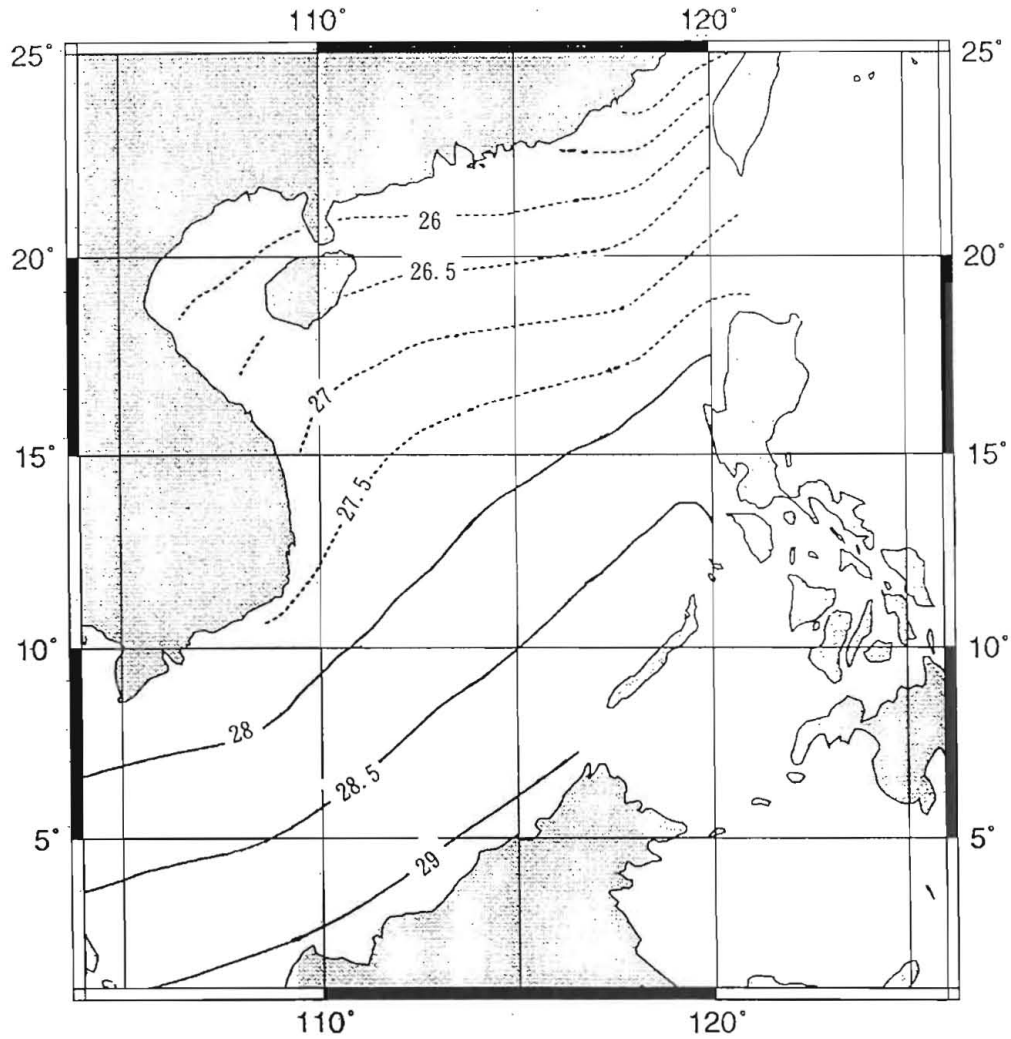

Figure 9. The Ensemble Mean SST Field (1964-84). The Solid (Dash) Lines Means SST Higher (Lower) than 28°C.

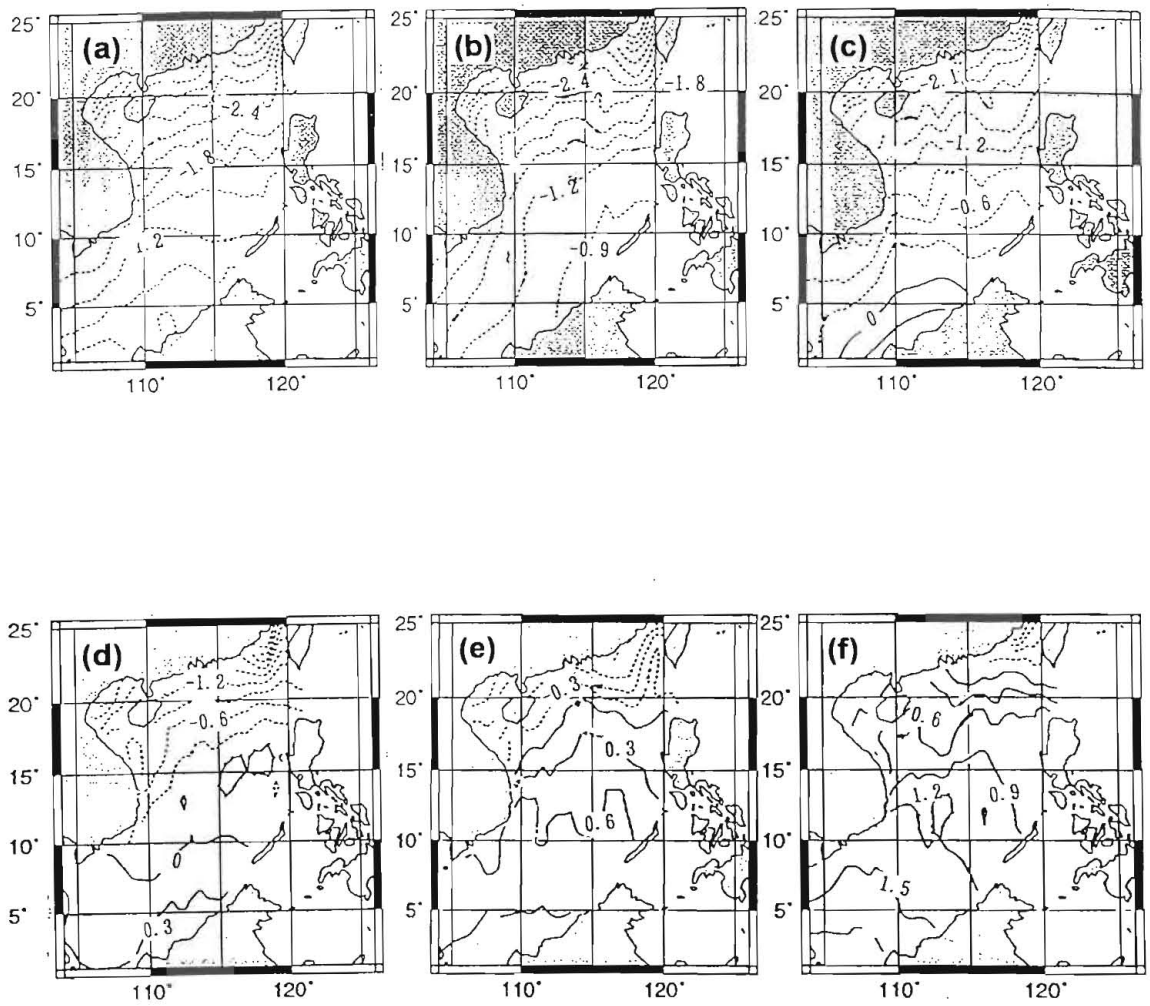

Figure 10. Average SST Anomalies Relative to the Ensemble Mean for (a) March 1-10, (b) March 11-20, (c) March 21-31, (d) April 1-10, (e) April 11-20, (f) April 21-30. Solid(Dash) Contours Denote Positive(Negative) Anomalies.

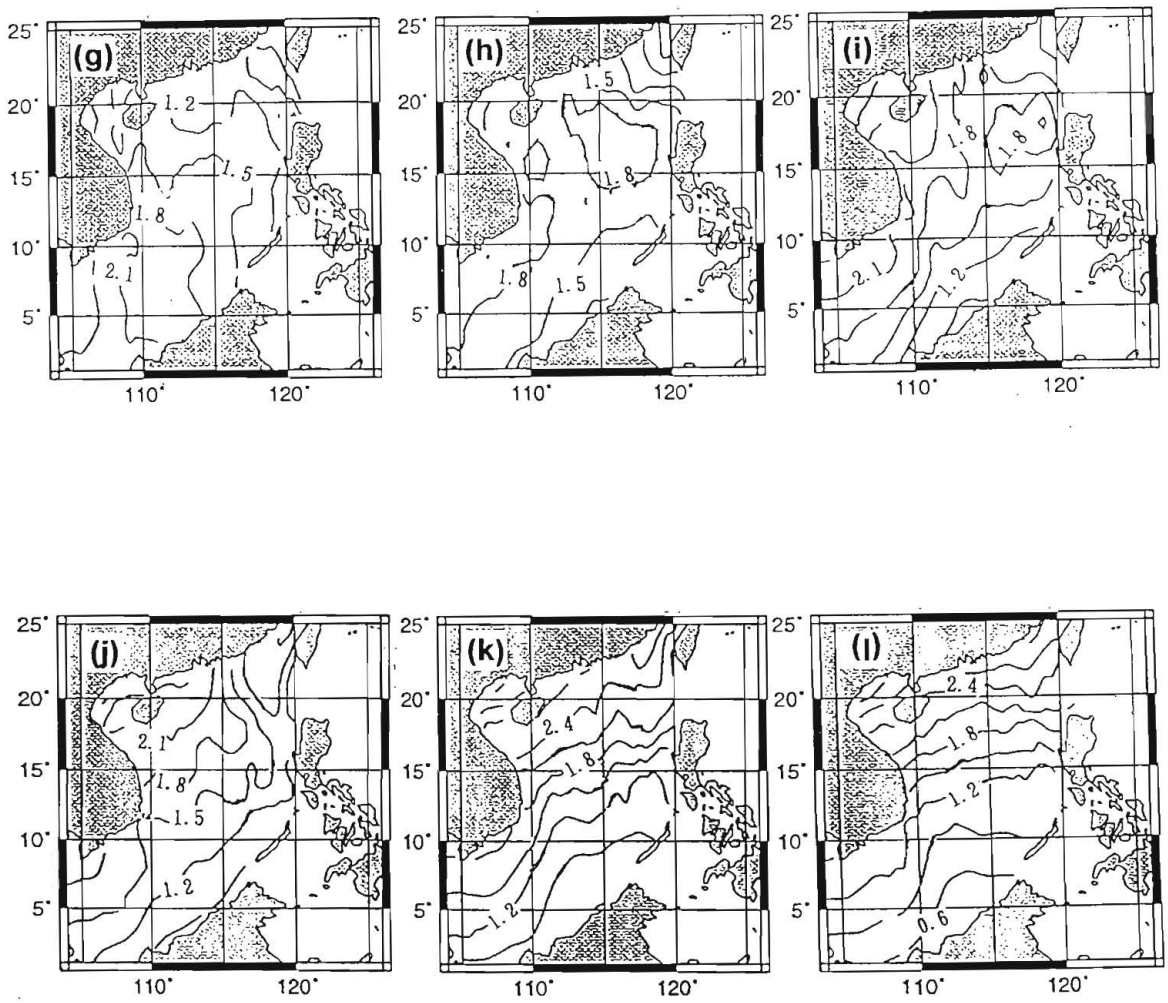

Figure 10. Average SST Anomalies Relative to the Ensemble Mean for (g) May 1-10, (h) May 11-20, (i) May 21-31, (j) June 1-10, (k) June 11-20, (l) June 21-30. Solid(Dash) Contours Denote Positive(Negative) Anomalies.

4. Mature Warming Phase

After the summer monsoon onset, the June $\widetilde{T}$ becomes positive almost everywhere throughout the whole SCS, and increases from the west coast of Borneo (≈0.6°C) to the southeast coast of China (≈2.4°C). This indicates that after the summer monsoon onset, the SCS warming is weakest near the Borneo coast and strongest near the Taiwan Strait (>2.4°C).

C. EMPRICAL ORTHOGONAL FUNCTION (EOF) ANALYSIS

The composite analysis demonstrated the existence of a central SCS warm-core eddy in the annual mean SST anomaly data. What are the transient features of this meso-scale eddy? What are the synoptic and interannual variabilities of the eddy? We can use the Emprical Orthogonal Function (EOF) technique to answer these questions.

1. EOFs for the SST Anomalies

The SST synoptic anomalies obtained by

$$\hat{T}(x_i, y_j, \tau_k, t_l) = T(x_i, y_j, \tau_k, t_l) - \overline{T}(x_i, y_j, t_l) \tag{10}$$

are re-arranged into a N×P matrix, $\hat{T}(r_n, \widetilde{t}_p), n = 1,2,\ldots,N$; and $p = 1,2,\ldots,P$. Here P = 756 is the total number of time points used for computing the covariance matrix, i.e., 21 years of every 10-day measurements; N = 255, corresponds to the number of grids ($i = 1,2,\ldots,17; j = 1,2,\ldots 15$). Lorenz (1956) used the eigenvectors of the covariance matrix associated with a sample data field to calculate the time series of coefficients or predictors for the statistical weather prediction. This method, called EOF analysis, separates the data sets into eigenmodes. Generally speaking, each mode has an associated variance, a non-dimensional spatial pattern, and a dimensional time series. From this data matrix a 255-square spatial covariance matrix is calculated by

$$R = \begin{bmatrix} R_{11} & R_{12} & \ldots & R_{1N} \\ R_{21} & R_{22} & \ldots & R_{2N} \\ \ldots & & & \\ R_{N1} & R_{N2} & \ldots & R_{NN} \end{bmatrix}, \quad R_{nm} = \sqrt{\frac{1}{p}\sum\nolimits_p \hat{T}(r_n, \widetilde{t}_p)\hat{T}(r_m, \widetilde{t}_p)}, \qquad N = 255 \tag{11}$$

where n and $m(1,2,\ldots,255)$ denote the grid locations. The diagonal elements of the covariance matrix $R_{nn} = (n = 1,2,\ldots,N)$ are the variance at location r_n. The off-diagonal elements are the covariance with spatial lag equal to the difference between the row and column indices. This symmetric matrix has its 255 real eigenvalues λ_α, and eigenvectors $\phi_\alpha(r_j)$ such that

$$\sum_{j=1}^{N} R_{ij}\phi_\alpha(r_j) = \lambda_\alpha\phi_\alpha(r_i), \qquad i = 1,2,\ldots N \tag{12}$$

The eigenvectors $\phi_1,\phi_2,\ldots,\phi_N$ are called Emprical Orthogonal Functions. Each ϕ_α is a 255-point (17×15 grid) distribution of SST anomaly pattern. The eigenvalues, $\lambda_\alpha(\alpha = 1,2,\ldots,N)$, are all positive and the summation of them, $\sum\lambda_\alpha$, equals the total variance. Therefore, λ_α is considered as the portion of total variance "explained" by the EOF ϕ_α. It is convenient to label the eigenfunctions ϕ_α so that the eigenvalues are in descending order, i.e.,

$$\lambda_1 > \lambda_2 > \lambda_3 > \ldots \tag{13}$$

2. Principal EOF Modes

Intraseasonal and interannual anomalies can be quantitatively investigated with the method of emprical orthogonal function (EOF) analysis and a number of its generalized forms. In order to delineate the major modes of variability in the winter and spring seasons (December to May) of 21 years (1964-84), we perform a conventional EOF analysis and obtain the first six leading EOFs. The first six leading EOF modes are able to account for 81.7% of the total variance during this season. They are summarized in Table 1. When combined, EOF1 and EOF2 explain over half (57%) of the total variance. Each EOF mode is normalized so that its total spatial variance is equal to unity. So, those patterns of the first six EOFs are enough to explain the spatial anomalies of whole SCS. Hence, it suffices to focus on the first six EOFs. Their structures are shown in Figure 11. Notice that the normalized EOF values are multiplied by 10.

EOF	Variance(%)	Accumulative Variance (%)
1	35.6	35.6
2	21.4	57.0
3	12.4	69.4
4	5.3	74.7
5	4.7	79.4
6	2.3	81.7

Table 1. Variances of the First Six Leading EOFs.

The EOF1 mode has an orderly homogeneous pattern of correlation and accounts for up to 35.6% of the total spatial variance during the winter and spring seasons (December to May). The NE - SW oriented isotherm pattern over this region is believed to be related to the ensemble mean pattern. The EOF2 (Figure 11b) mode shows a strong eddy pattern with a closed isoline of -4°C (actual value is -0.4°C) to the west of Luzon Island (116°-119°E, 16°-19°N) and accounts for about 21.4% of variance. The size of the eddy is around 100,000 km^2. However, we still cannot identify whether the eddy in EOF2 represents a warm or cold ring since the values in Figure 8 are normalized. We must therefore examine the products of the EOF values and the corresponding time series of the amplitudes.

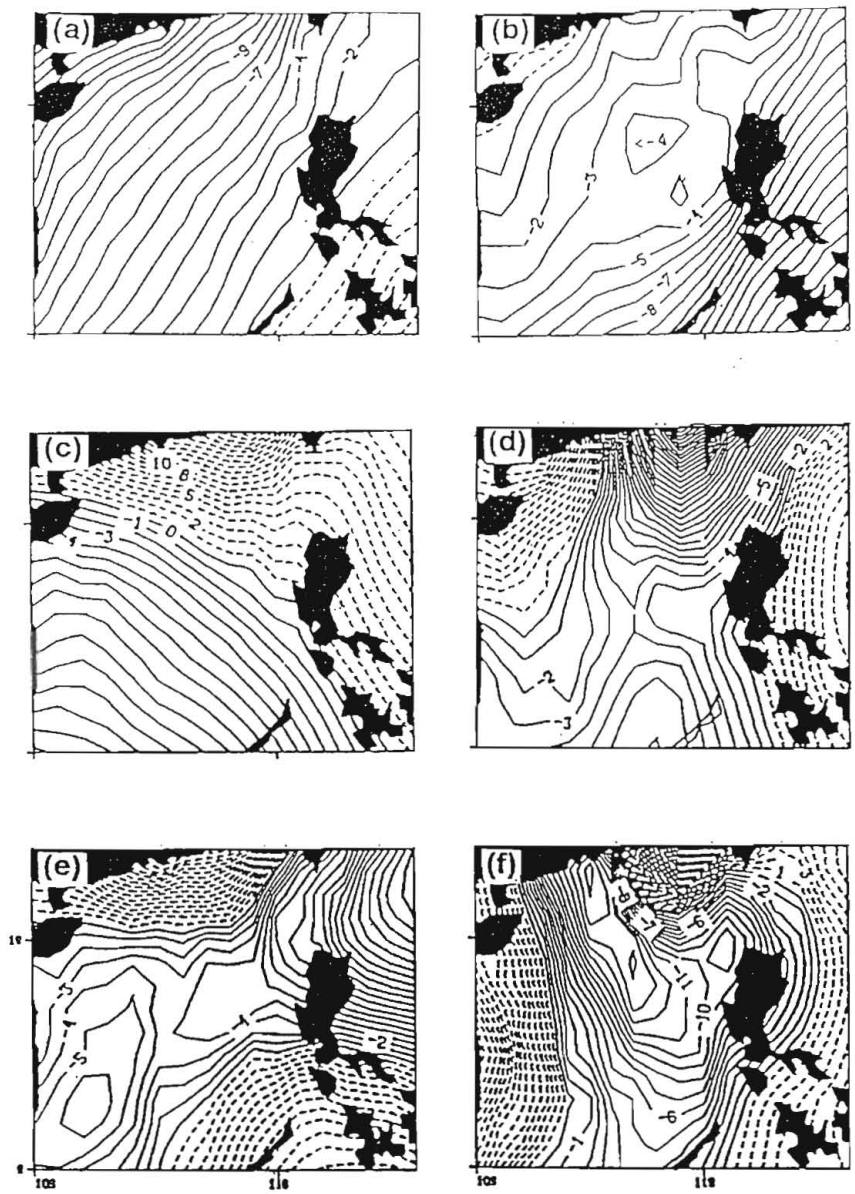

Figure 11. The First Six EOF Modes for the SST Anomalies (°C) Computed From December-May During 1964-84; (a) EOF1, (b) EOF2, (c) EOF3, (d) EOF4, (e) EOF5, (f) EOF6. The EOF Model Values have been Multiplied by 10.

3. Temporal Variabilities

The data matrix, $\hat{T}(r_n, \tilde{t}_p)$ is approximately written by

$$\hat{T}(r_n, \tilde{t}_p) = \sum_\alpha B_\alpha(\tilde{t}_p)\phi_\alpha(r_n) \tag{14}$$

where $B_\alpha(\tilde{t}_p)$ is a set of time series of size P, representing the temporal variation of the associated spatial pattern described by EOF $\phi_\alpha(r_n)$. The result of the time series seems to be a projection of the SST anomaly through a 'filter' of EOF modes during a time scale.

The time series of EOF1 amplitudes $B_1(\tilde{t}_p)$ for 1964-84 are shown in Figure 12. The EOF1 mode $\phi_1(r_n)$ is always negative throughout the whole South China Sea (Figure 11a). Therefore, $B_1(\tilde{t}_p) > 0$, corresponds to negative SST anomalies, and $B_1(\tilde{t}_p) < 0$, corresponds to positive SST anomalies. Taking the year of 1968 as an example, $B_1(\tilde{t}_p)$ is always positive from early January to early May, which implies negative SST anomalies in the whole SCS during this period. Furthermore, the strength of the negative SST anomalies is weak near the west coast of Borneo and increases northwestward towards the southeast coast of China (Figure 11a).

The time series of EOF2 amplitudes $B_2(\tilde{t}_p)$ for 1964-84 are shown in Figure 13. The EOF2 mode $\phi_2(r_n)$ (Figure 11b) is almost negative throughout the whole SCS except near Hainan Island and shows a strong eddy with closed isoline of -4°C to the west of Luzon Island. As before, $B_2(\tilde{t}_p) > 0$, corresponds to negative SST anomalies (or a cold-core eddy), and $B_2(\tilde{t}_p) < 0$, corresponds to positive SST anomalies (or a warm-core eddy). Taking the year of 1964 as an example, $B_2(\tilde{t}_p)$ is almost always negative from early January to early May and reaches a minimum value (-15) in 1-10 April, which implies positive SST anomalies over the whole SCS and a warm-core eddy to the west of Luzon Island during the 1964 winter and spring seasons. The strength of the warm-core eddy increases from February to April. The SST anomaly of the warm-core eddy in April is around 6°C (-0.4°C × -15). The actual SST anomaly (6°C) is the product of the

second EOF mode (-0.4°C) and its corresponding amplitude (-15). On the other hand, taking the year of 1972 as another example, $B_2(\tilde{t}_p)$ is almost always positive from early January to early May with a mean value around 3, which implies negative SST anomalies over the whole SCS and a cold-core eddy to the west of Luzon Island during 1972 winter and spring seasons. The strength of the cold-core eddy fluctuates from January to May. The SST anomaly of the cold-core eddy in 1972 is around -1.2°C (-0.4°C × 3).

D. SCS COLD-CORE EDDY DURING EL NIÑO YEARS

From the above analysis, we see a different thermal behavior in the central SCS between the 1964 and 1972 winter monsoon seasons: a warm-core eddy in 1964 and a cold-core eddy in 1972. What might cause this interannual variability? Initially, one might think of a change in the large-scale surface atmospheric circulation. A reasonable guess is the El Niño event (1972 is an El Niño year). During an El Niño year, the monsoon circulation was greatly weakened (Kuo, 1989). The wind stress curl over the SCS might be different between non-El Niño and El Niño years. Following this line of reasoning, we averaged the amplitudes of EOF1 and EOF2 for El Niño years and non-El Niño years, respectively. The set of El Niño years consists of 1965, 1969, 1972, 1976, 1982, and 1983, and the set of non-El Niño years includes the rest of the years. The mean fields for non-El Niño years generally may represent conditions closer to the climatological mean. The averaged amplitudes of EOF1 of non-El Niño years indicate positive values from February to March (Figure 14a), which implies negative SST anomalies over all the SCS during this period. Furthermore, the strength of the negative SST anomalies is weak near the west coast of Borneo and increases northwestward towards the southeast coast of China. Conversely, the averaged amplitudes of EOF1 of El Niño years are negative values (Figure 14b). Its SST anomaly pattern is opposite to the pattern of the non-El Niño years during this period of time.

The averaged amplitudes of EOF2 of non-El Niño years indicate negative values during the whole winter and spring seasons (Figure 15a), which implies positive SST

anomalies over all the SCS and a warm-core eddy to the west of Luzon Island during this period. However, the averaged amplitudes of EOF2 during El Niño years indicate positive values during the whole winter and spring seasons (Figure 15b), which implies negative SST anomalies over all the SCS and a cold-core eddy to the west of Luzon Island during this period. The averaged amplitude is usually smaller than individual years. This implies that a SCS warm-core eddy appears frequently from January to May during non-El Niño years.

Our data set also shows that during El Niño years a cold-core eddy will frequently appear from January to May in the central SCS (Figure 15b). After relating the difference in the SST anomaly pattern to non-El Niño and El Niño years, we believe that the appearance of a warm-core or a cold-core eddy is related to the global atmospheric circulation.

E. SCENARIOS FOR THE CENTRAL SCS EDDY FORMATION

The MOODS data set shows that during boreal winter and spring a warm-core eddy often appears in the central SCS except for El Niño years when a cold-core eddy usually appears. To examine this further, we use climatological data sets such as the monthly mean surface wind stress data (Hellerman and Rosenstein, 1983) and monthly mean temperature and salinity data sets (Levitus, 1982) to study the eddy formation mechanisms in non-El Niño years since the mean features of the non-El Niño years are more likely closer to the climatology.

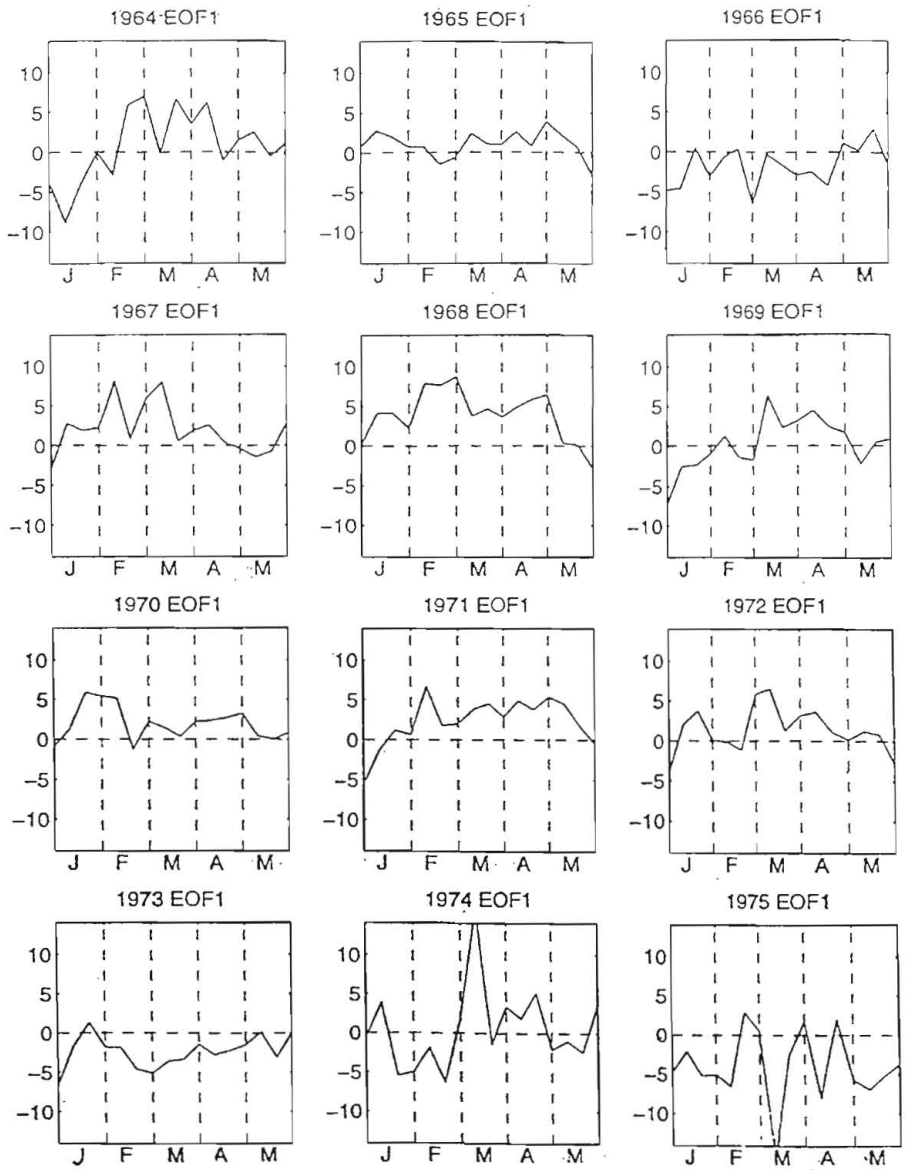

Figure 12. Time Series of EOF1 Amplitudes (January to May) for 1964-75.

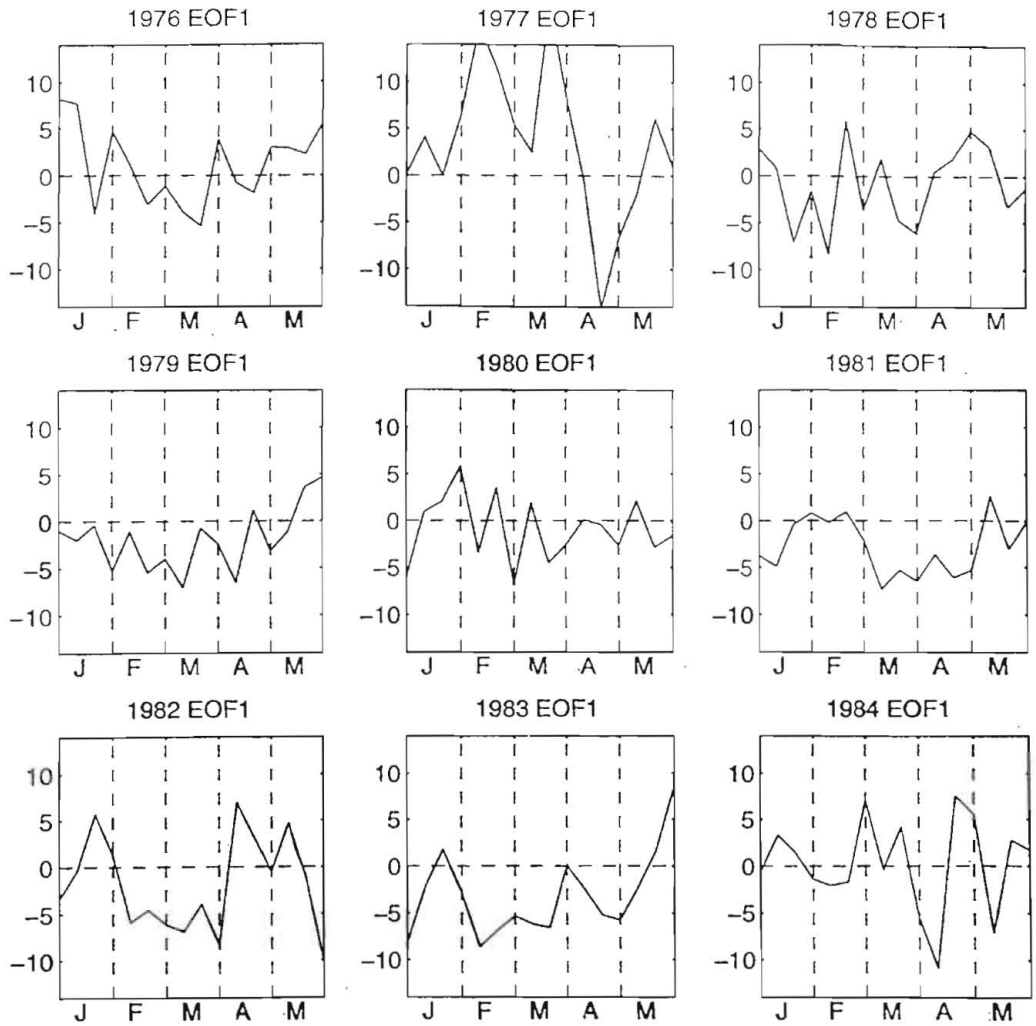

Figure 12. Time Series of EOF1 Amplitudes (January to May) for 1976-84.

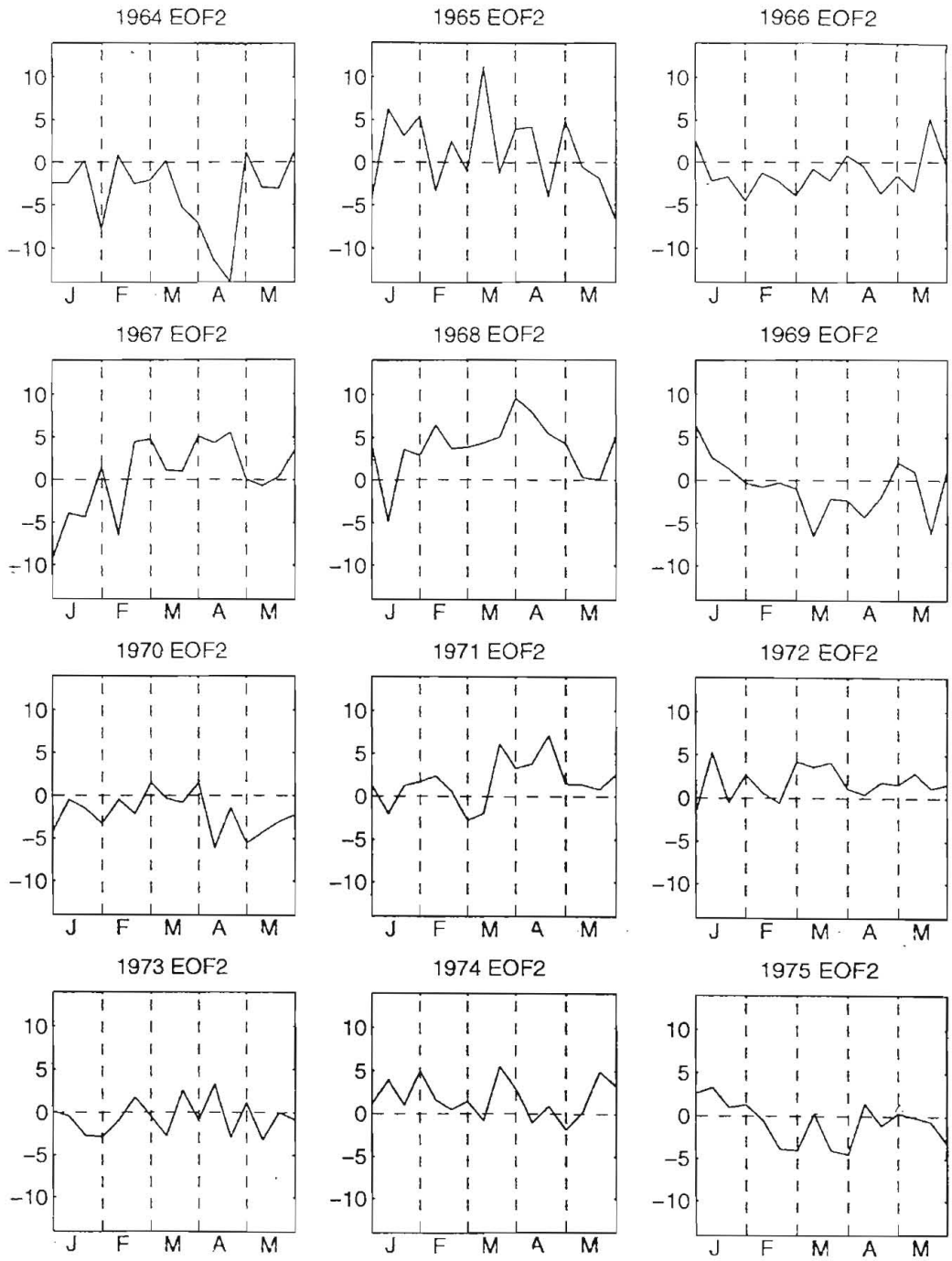

Figure 13. Time Series of EOF2 Amplitudes (January to May) for 1964-75.

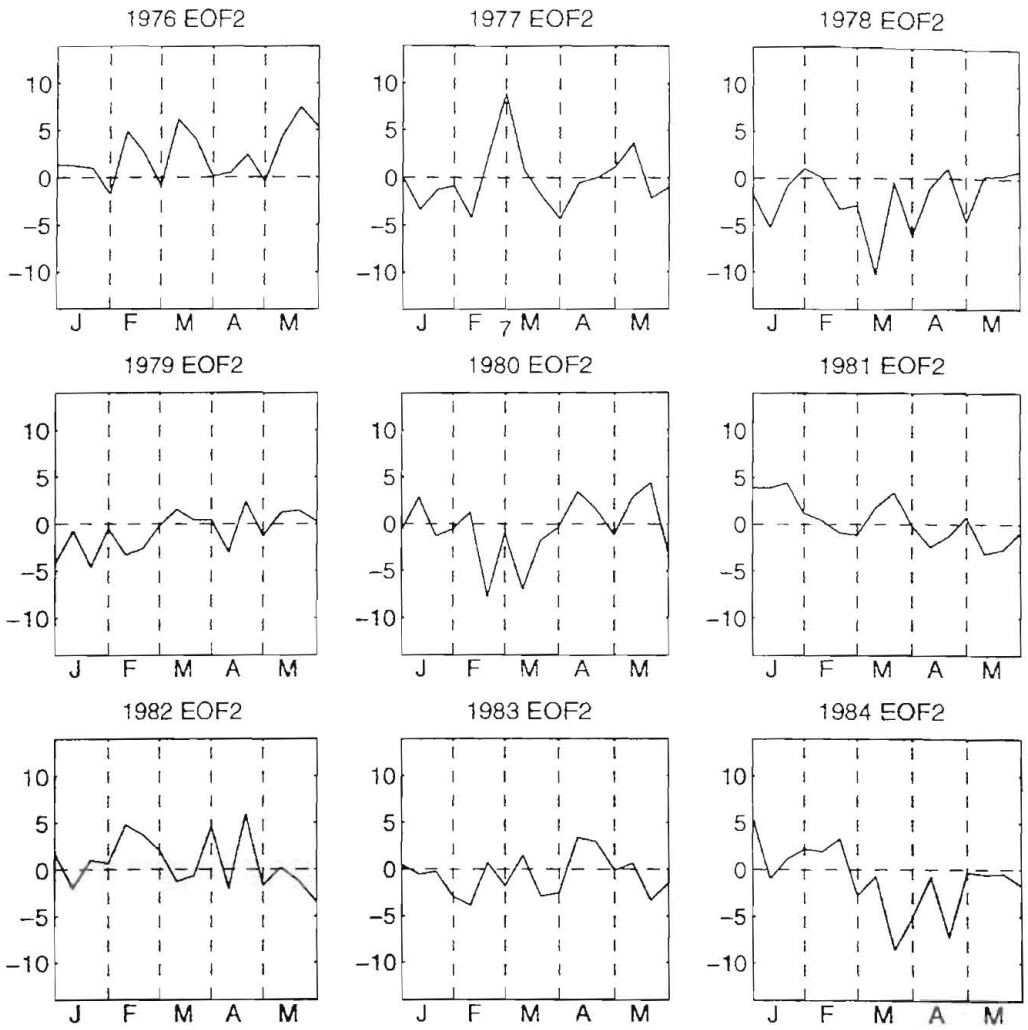

Figure 13. Time Series of EOF2 Amplitudes (January to May) for 1976-84.

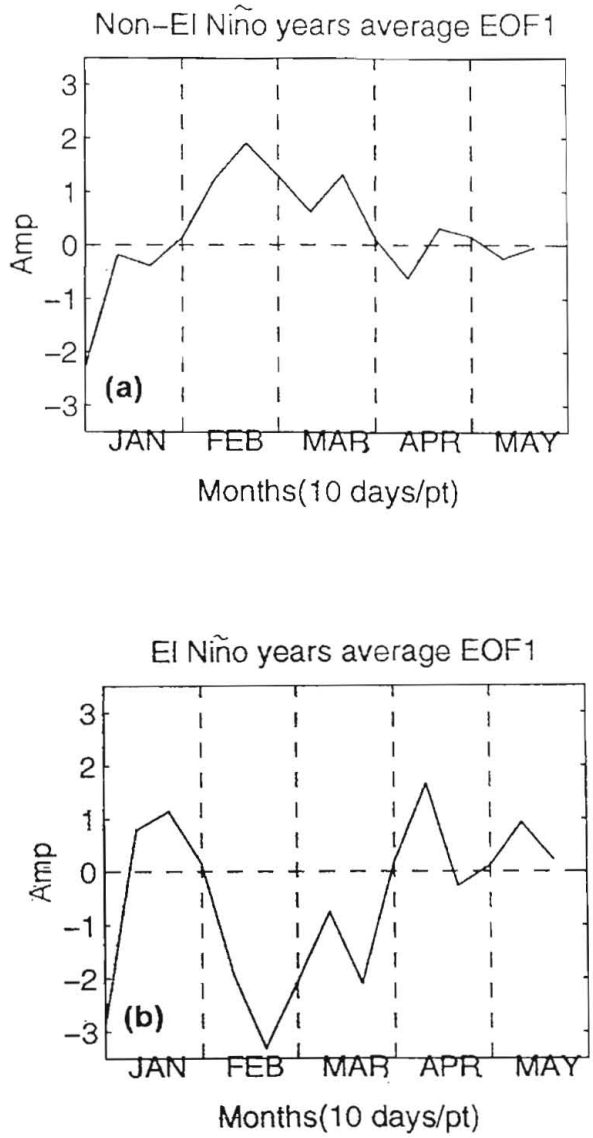

Figure 14. Time Series (January to May) of EOF1 Amplitudes Averaged Anomaly: (a) Non-Niño Years, (b) and El Niño Years (1965, 1969, 1972, 1976, 1982, 1983).

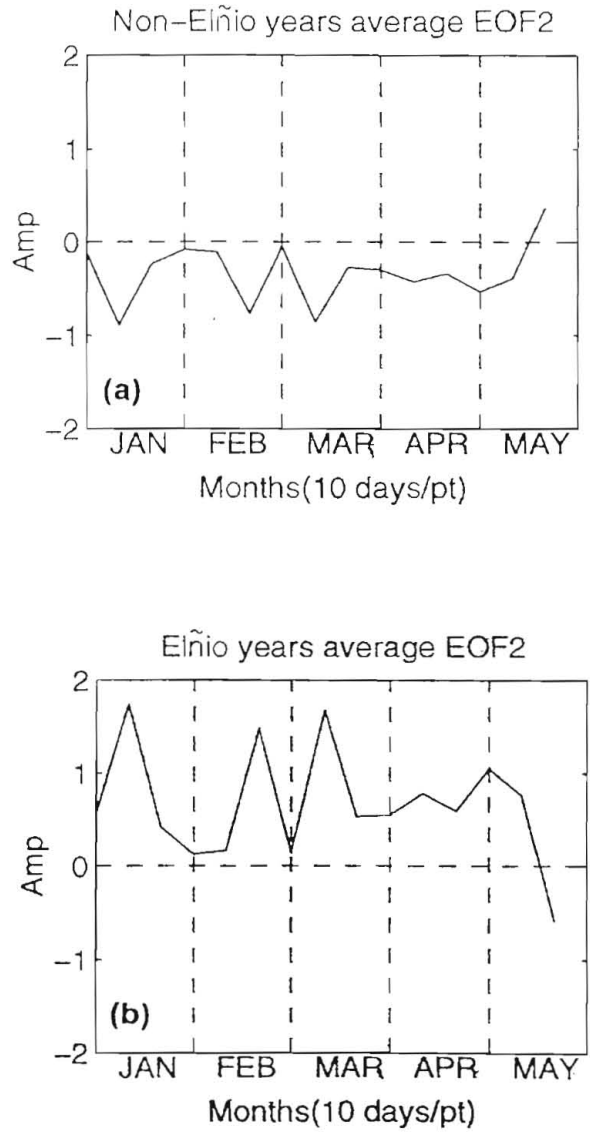

Figure 15. Time Series (January to May) of EOF2 Amplitudes Averaged Anomaly: (a) Non-Niño Years, (b) and El Niño Years (1965, 1969, 1972, 1976, 1982, 1983).

We try to answer the following questions: What is the mechanism for a warm-core eddy formation under climatological conditions (more likely representing non-El Niño years)? What is the difference of the surface forcing over the SCS between non-El Niño and El Niño years? What is the mechanism for a cold-core eddy formation in El Niño years?

Two possible mechanisms may explain the central SCS warm-core eddy formation during the winter monsoon season: (1) the effects of downwelling, and (2) the Kuroshio intrusion. Figure 10d indicates that the early SCS warming starts at the central and south SCS, not at the Luzon Strait. This implies that the Kurushio intrusion is not a key factor to cause the central SCS warm-core eddy formation. Therefore, the downwelling effect is the predominant mechanism for the central SCSWP formation in the boreal winter and spring.

1. Ekman Pumping in Central SCS

The monthly climatological wind data (Hellerman and Rosenstein, 1983) over the SCS and adjacent areas were used to compute the Ekman pumping velocity (Figures 16-19).

$$w_E = \frac{1}{p}\left[\frac{\partial}{\partial x}\left(\frac{\tau_y}{f}\right) - \frac{\partial}{\partial_y}\left(\frac{\tau_x}{f}\right)\right] \tag{15}$$

Here (τ_x, τ_y) are the surface wind stresses. Figures 16-19 shows the Ekman pumping velocity by the color contours for March-June. The arrows indicate the surface wind stress. We see that during March-May (Figure 16-18) a downwelling region with a vertical velocity around -0.025 cm/s appears in the central SCS. After the summer monsoon onset (June), the surface winds change direction, and a weak upwelling area with vertical velocity around 0.005 cm/s appears in the central SCS between 14°N and 19°N (Figure 19).

2. Thermal Feature of the Central SCS

Figure 20 shows two sets of April MOODS temperature profiles. One is for 1968 (a non-El Niño year), and the other is for 1982 (an El Niño year). The central SCS water is always highly stratified before the summer monsoon onset.

The ocean mixed layer temperature is much higher than the sublayer temperature. The Ekman downwelling in the central SCS during the winter and spring seasons will suppress the vertical cold advection from the sublayer. This downwelling effect, plus the increase in solar radiation in spring (April-May), may provide some important pre-conditions for the central SCS warm-core eddy formation.

3. An Air-Sea Feedback for a Warm-Core Eddy (Non-El Niño)

We propose an air-sea feedback scenario for the central SCS warm-core eddy formation in non-El Niño years (Figure 21). From late winter to spring, an anticyclone appears in the central SCS from the ensemble mean atmospheric surface streamline analysis (Figure 22a). This anticyclone generates downwelling in the central SCS and in turn prevents the cold deep water from being advected to the surface. This will promote the formation of the warm-core eddy in the central SCS. As the central SCS warm-core eddy persists, being around 1 °C warmer than the surroundings, an atmospheric surface low pressure center will be generated above the warm water, which may trigger the summer monsoon onset.

After the summer monsoon onset, an atmospheric surface cyclone will occupy the central SCS (Figure 22b). This cyclone will generate upwelling in the central SCS, which entrains the deep cold water into the surface mixed layer. This upwelling effect will finally destroy the central SCS warm-core eddy.

During El Niño events, the Asian monsoon circulation is greatly weakened (Kuo, 1989) and so will be the downwelling effect. Therefore, the warm-core eddy is not likely to occur in the boreal winter and spring during El Niño events. The mechanism for a cold-core eddy formation in El Niño years should be further studied.

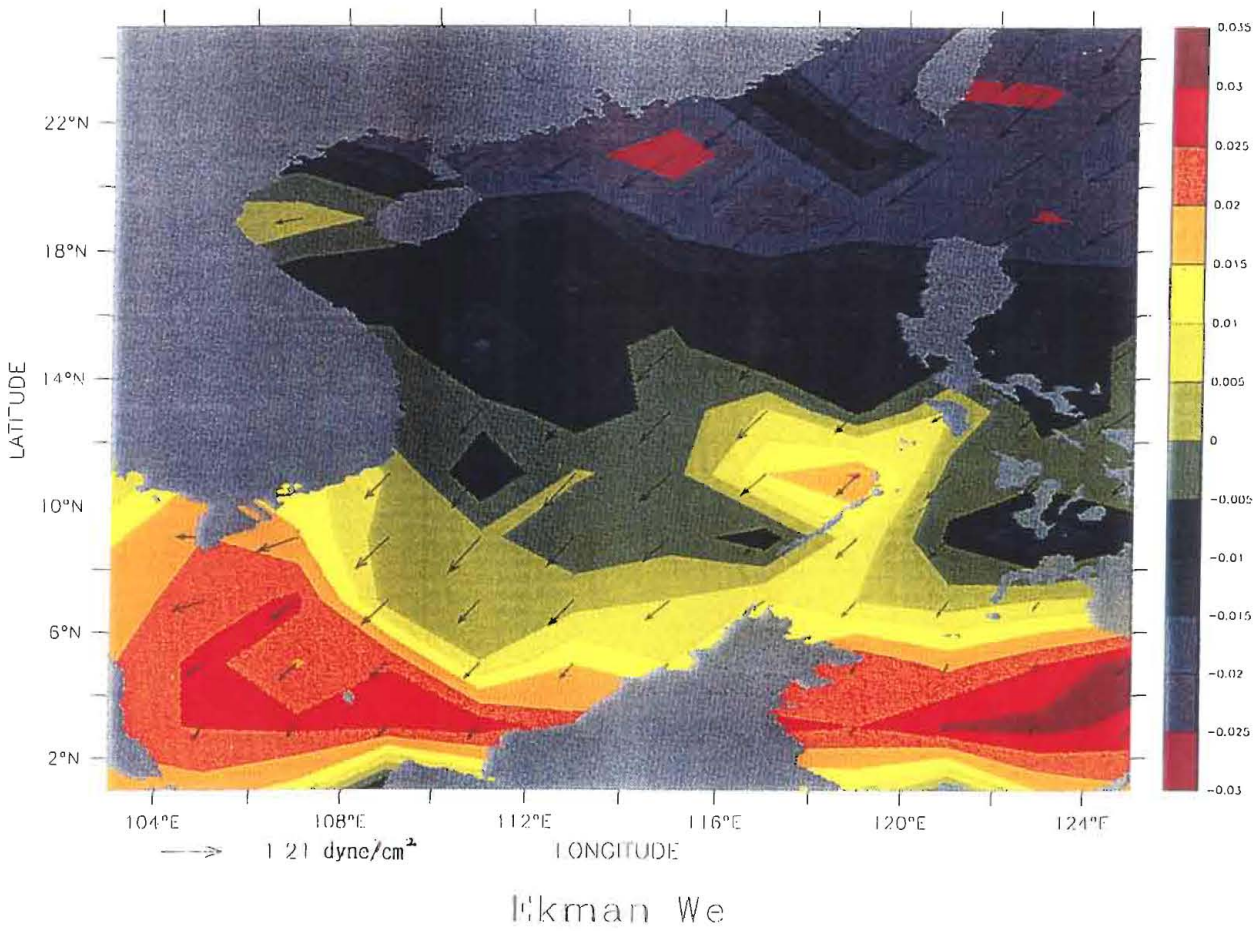

Figure 16. The Ekman Pumping Velocity During March. The Colors Associated With Positive (Negative) Values Indicate Upwelling (Downwelling) (cm/s). The Arrows Denote the Mean Wind Stresses (From Hellerman and Rosenstein, 1983).

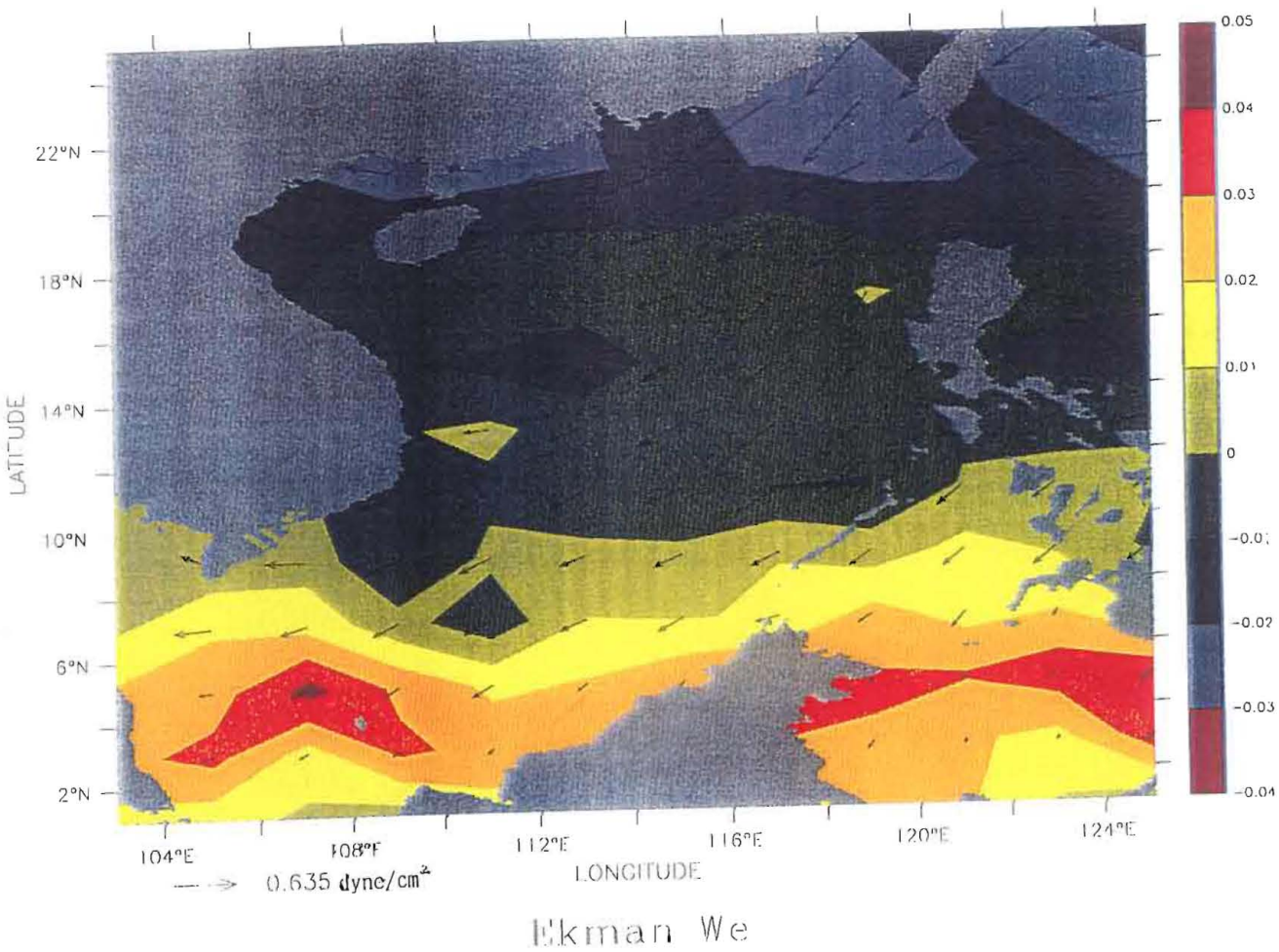

Figure 17. The Ekman Pumping Velocity During April. The Colors Associated With Positive (Negative) Values Indicate Upwelling (Downwelling) (cm/s). The Arrows Denote the Mean Wind Stresses (From Hellerman and Rosenstein, 1983).

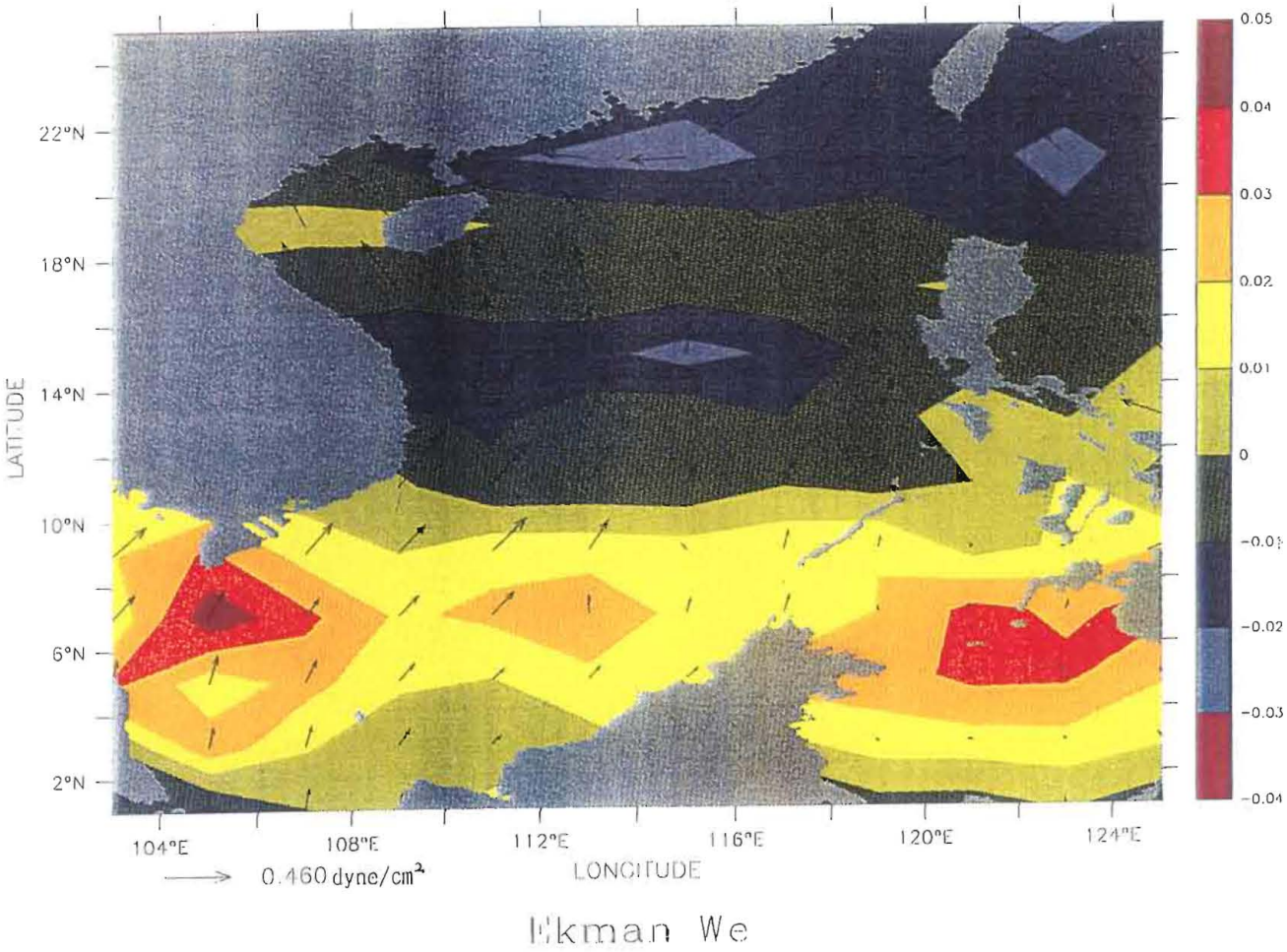

Figure 18. The Ekman Pumping Velocity During May. The Colors Associated With Positive (Negative) Values Indicate Upwelling (Downwelling) (cm/s). The Arrows Denote the Mean Wind Stresses (From Hellerman and Rosenstein, 1983).

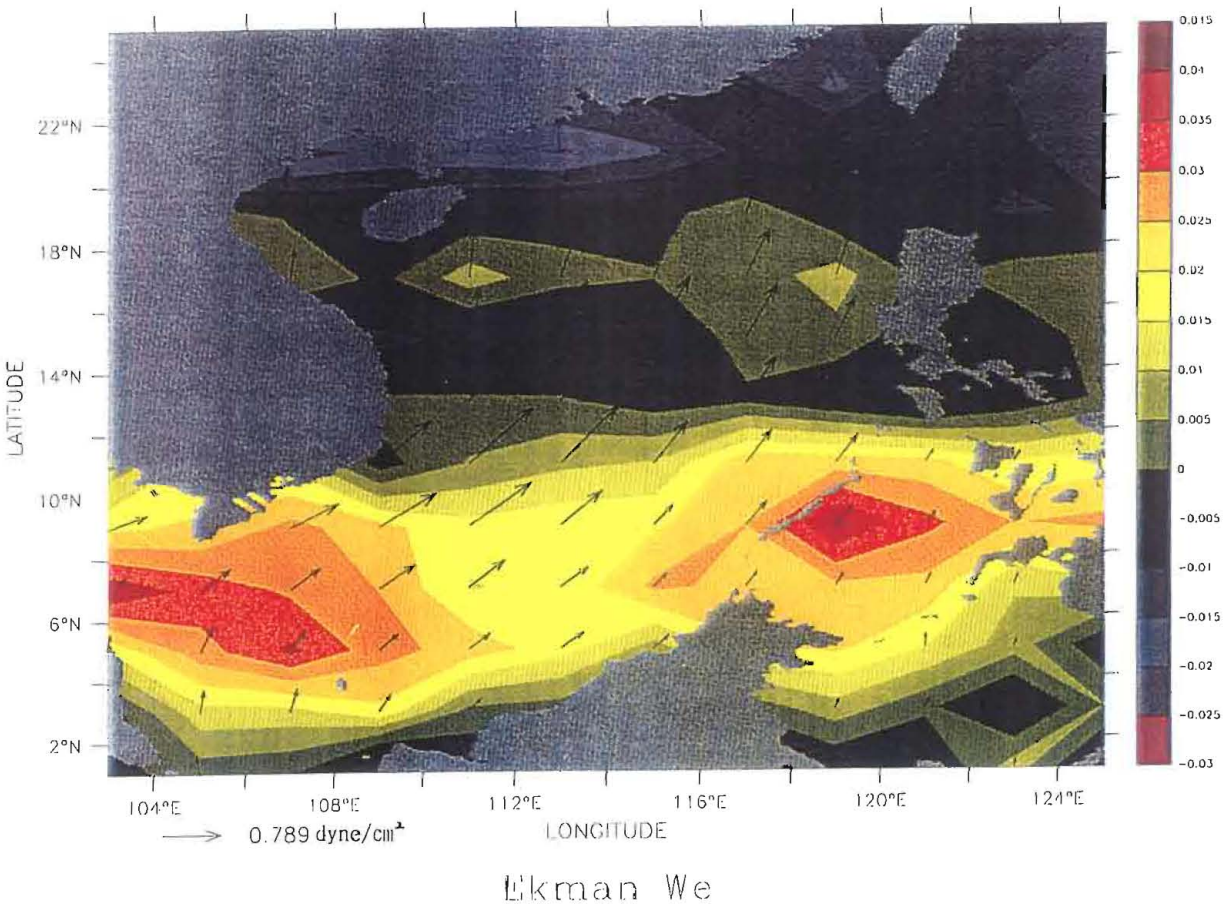

Figure 19. The Ekman Pumping Velocity During June. The Colors Associated With Positive (Negative) Values Indicate Upwelling (Downwelling) (cm/s). The Arrows Denote the Mean Wind Stresses (From Hellerman and Rosenstein, 1983).

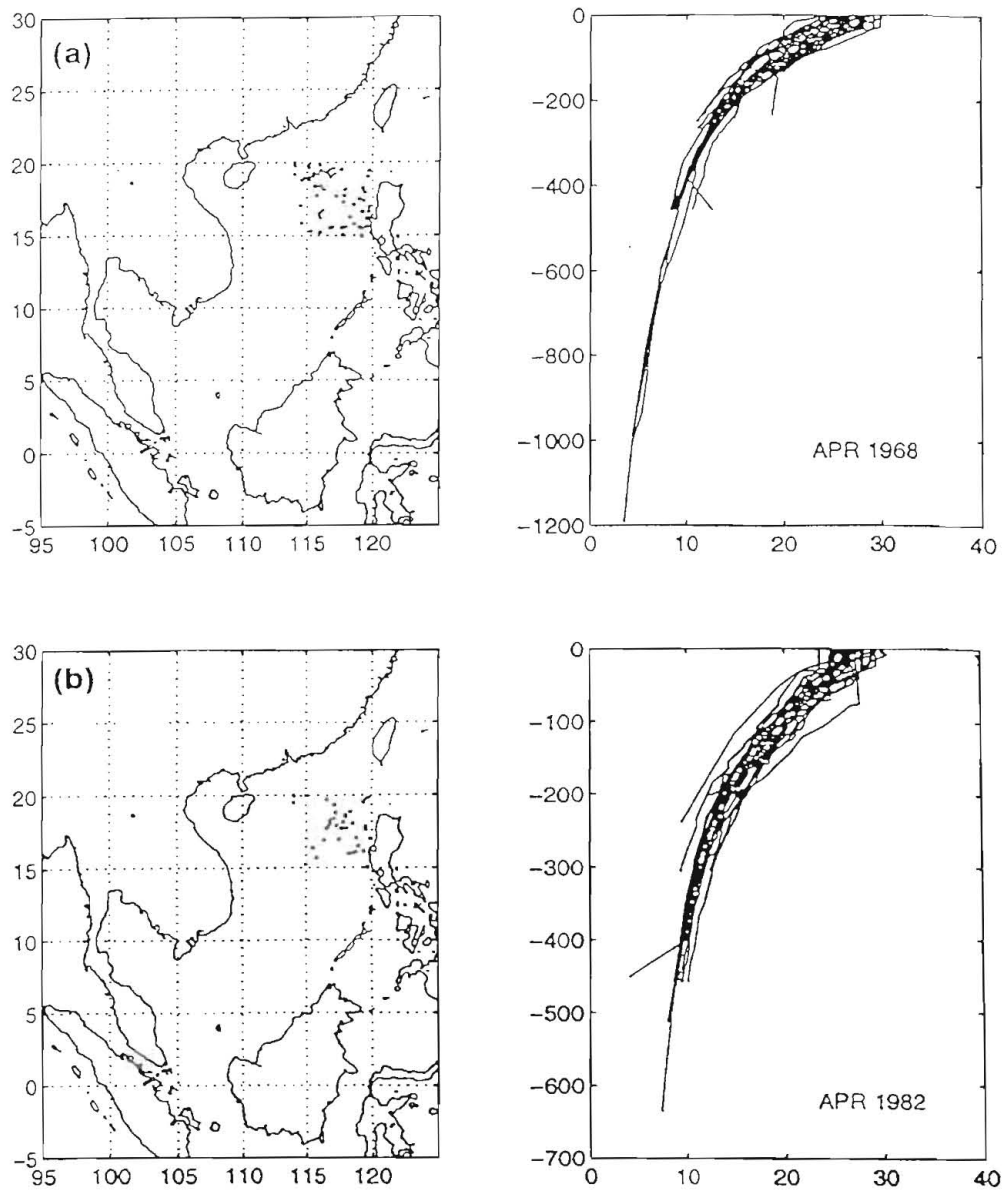

Figure 20. Selected MOODS Temperature Profiles for (a) April 1968, and (b) April 1982.

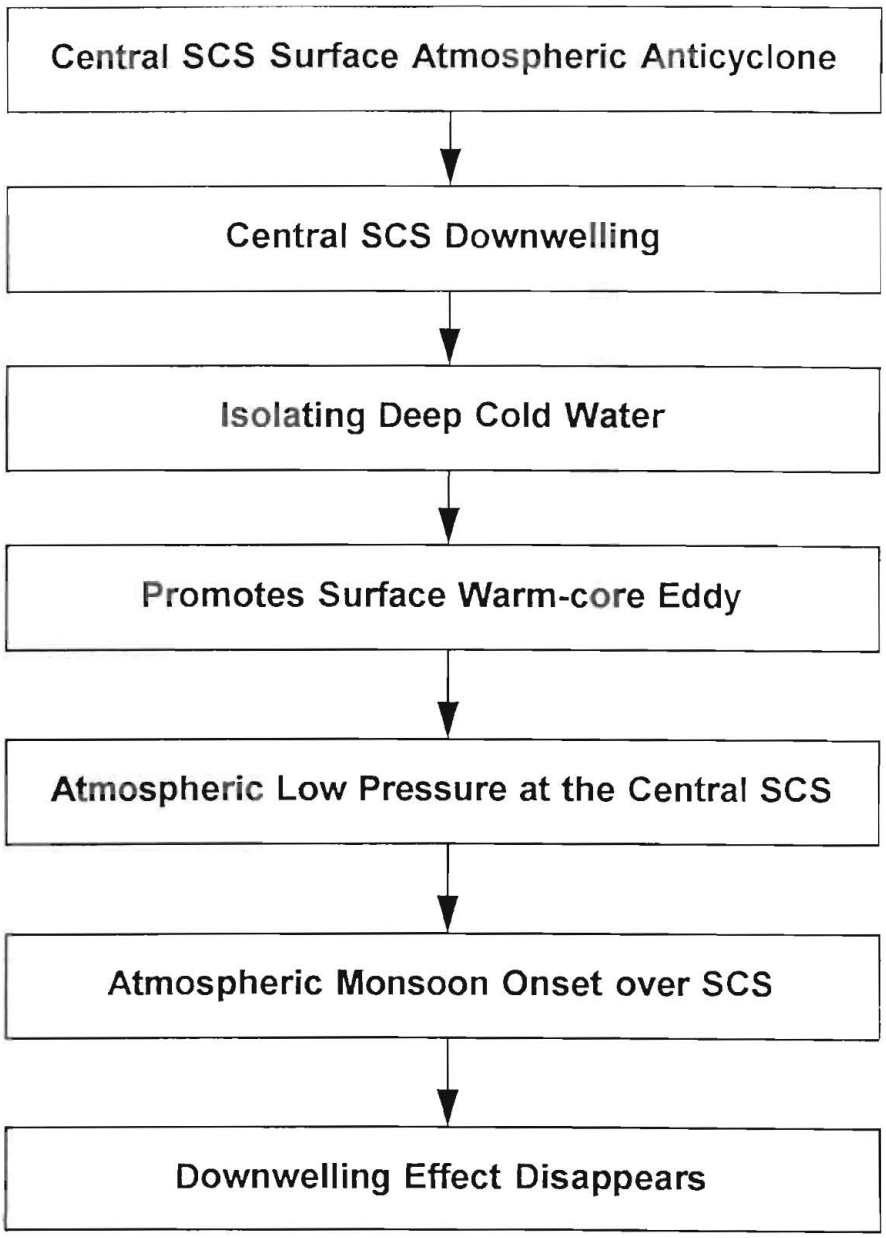

Figure 21. An Air-Sea Feedback Scenario for the SCS Warm-Core Eddy Life Cycle.

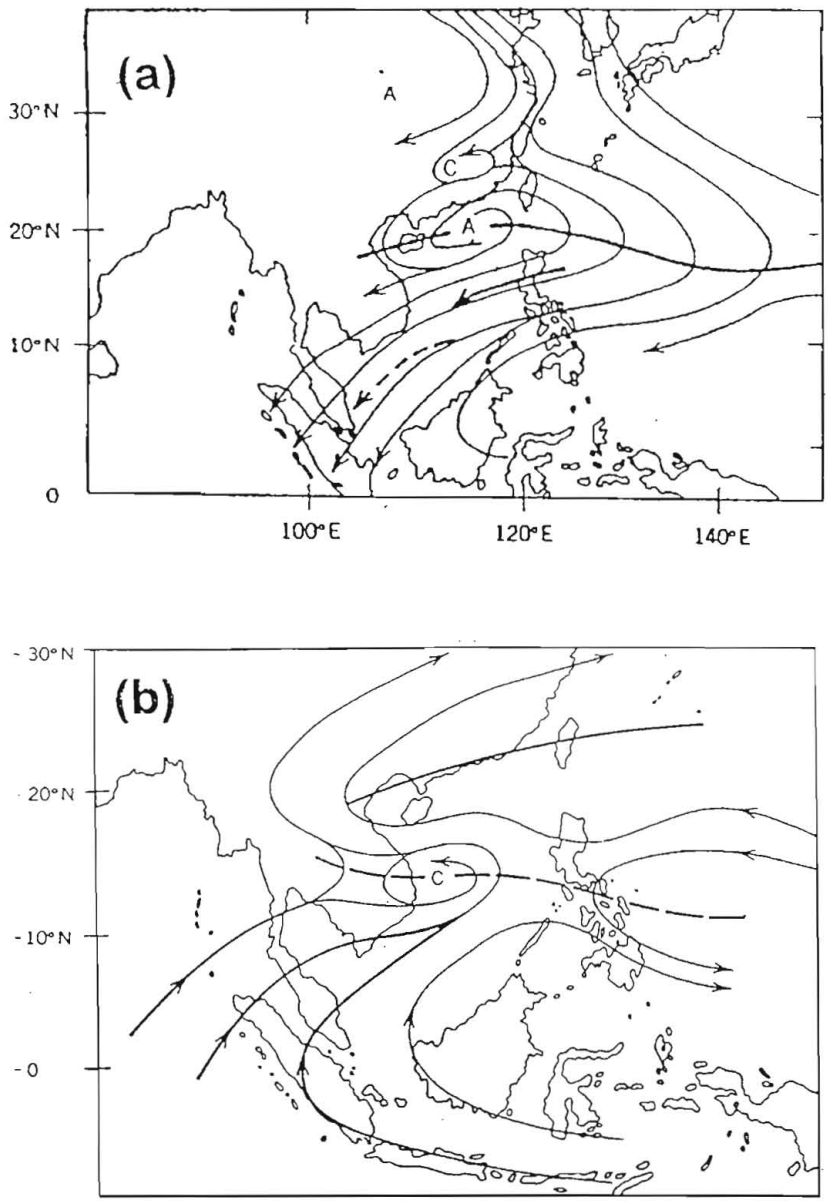

Figure 22. Mean Atmospheric Surface Streamline Analysis for (a) Early Spring, and (b) Summer (From Cheang, 1980).

IV. NUMERICAL SIMULATIONS

We use a numerical model to simulate the formation of the central SCS warm-core eddy. Through this simulation, we hope to verify the downwelling effect scenario.

A. PRIMITIVE EQUATION MODEL

The model we use is the three dimensional model developed by Blumberg and Mellor (1983, 1987) with the hydrostatic and Boussinesq approximations (Bryan, 1969) and has the following features: (1) horizontal curvilinear coordinates and an "Arakawa C" scheme (Arakawa and Lamb, 1977), (2) sigma coordinates in the vertical with realistic bathymetry, (3) a free surface, (4) a second-order turbulence closure model for the vertical viscosity (Mellor and Yamada, 1974, 1982), (5) horizontal diffusivity coefficients calculated by the Samagorinsky (1963) parameterization, and (6) split time steps for barotropic and baroclinic modes. The basic equations are given by

$$\frac{\partial u}{\partial t} + V \circ \nabla u + w\frac{\partial u}{\partial z} - fv = -\frac{1}{\rho_o}\frac{\partial p}{\partial x} + \frac{\partial}{\partial z}(K_M \frac{\partial u}{\partial z}) + F_x \tag{16}$$

$$\frac{\partial v}{\partial t} + V \circ \nabla v + w\frac{\partial v}{\partial z} - fu = -\frac{1}{\rho_o}\frac{\partial p}{\partial y} + \frac{\partial}{\partial z}(K_M \frac{\partial v}{\partial z}) + F_y$$

$$\rho g = -\frac{\partial p}{\partial z}$$

$$\nabla \circ V + \frac{\partial w}{\partial z} = 0$$

$$\frac{\partial \theta}{\partial t} + V \circ \nabla \theta + w\frac{\partial \theta}{\partial z} = \frac{\partial}{\partial z}(K_H \frac{\partial \theta}{\partial z}) + F_\theta$$

$$\frac{\partial S}{\partial t} + V \circ \nabla S + w\frac{\partial S}{\partial z} = \frac{\partial}{\partial z}(K_H \frac{\partial S}{\partial z}) + F_S$$

where $V = (u, v)$ is the horizontal velocity, w the vertical velocity, and g the gravitational acceleration. ρ_o is the characteristic density, ρ the in situ density, θ the temperature, S the salinity, p the pressure, (K_M, K_H) the vertical eddy diffusivities for turbulent mixing

of momentum (K_M) and temperature and salinity (K_H), $(F_x, F_y, F_\theta, F_S)$ the horizontal mixing terms representing the subgrid scale processes. The density ρ is computed by the equation of state of the form

$$\rho = \rho(\theta, S) \tag{17}$$

given by Fofonoff (1962).

The model domain is 99°E-121°E, 3°S-25°N which includes the South China Sea and the Gulf of Thailand. With its 20 km horizontal resolution and 23 vertical sigma coordinate levels, it has 125×162×23 grid points (Figure 23). All depths less than 10 m in the domain are set to be 10 m in order to satisfy the constraint $H + \eta > 0$. In the vertical the domain is divided into 23 levels $\sigma_n (n = 1,2,\ldots,23)$. Here $\sigma_n = n\Delta\sigma, \Delta\sigma = -1/23$. In the simulation, we use the Samagorinsky parameterization to compute the horizontal mixing coefficients with C=0.1, which results in the horizontal viscosity ranging from 200 to 500 $m^2 s^{-1}$. The background vertical mixing coefficient is 10^2 $m^2 s^{-1}$ (Blumberg and Mellor, 1983, 1987).

B. LATERAL BOUNDARY CONDITIONS

There are several major straits connecting the SCS to the Pacific Ocean and surrounding seas. Many are very shallow (i.e., the Strait of Malacca) or irregular (i.e., the Balabac Strait) and difficult to be adequately represented in a numerical model. Therefore, we close the Strait of Malacca, and all the small straits between Luzon Island and Borneo in the numerical model. We combine the Karimata Strait and the Gasper Strait into one open boundary. After this treatment, our model has three open boundaries: a northern boundary (Taiwan Strait), an eastern boundary (Luzon Strait), and a southern boundary (Karimata-Gasper Strait). The transports at the three open boundaries were determined according to Wyrtki's (1961) estimation with some modification due to the boundary treatment. Table 2 shows the seasonal variation of the transport

$(1sv \equiv 10^6 m^3 s^{-1})$ at the three open boundaries. The summation of the total transport through the open boundaries is always zero in order to satisfy mass conservation.

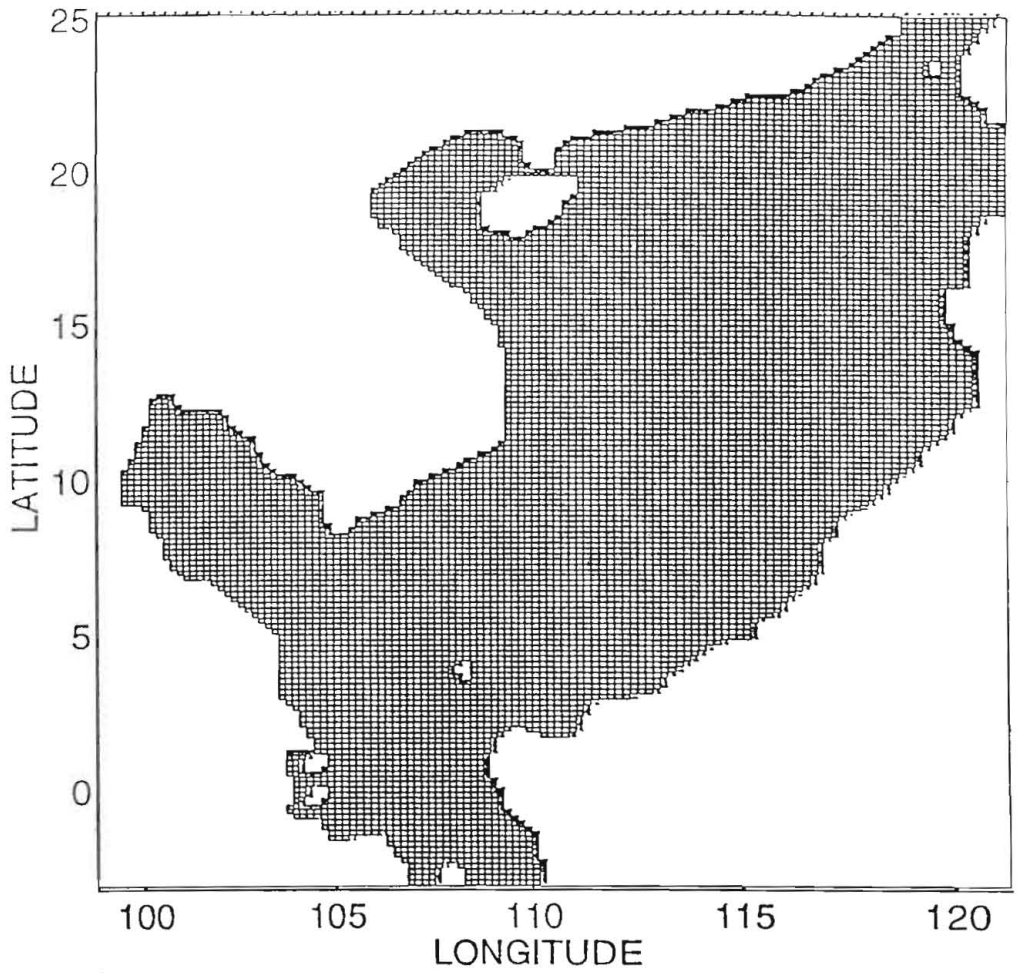

Figure 23. Model Domain of South China Sea with 20 km × 20 km Grids.

Month	Feb.	Apr.	Jun.	Aug.	Oct.	Dec.
Gasper & Karimata Straits (Eastward Positive)	4.4	0.0	-4.0	-3.0	1.0	4.3
Luzon Strait (Eastward Positive)	-3.5	0.0	3.0	2.5	-0.6	-3.4
Formosa Strait (Northwards Positive)	-0.9	0.0	1.0	0.5	-0.4	-0.9

Table 2. The Bi-monthly Variation of Mass Transport (Sv) at The Open Boundaries. The Values were Taken from Wyrtki (1961).

The barotropic velocity at the open boundaries V_n^{BT} is obtained by

$$V_n^{BT} = \frac{Transport}{\int_l hdl} \tag{18}$$

where l is the boundary width, and n means the normal direction to the boundary. The baroclinic velocity, $V_n^{BC}(\sigma)$ is calculated by

$$V_n^{BC}(\sigma) = V_n^{BT} \frac{e^{\sigma}}{1-e^{-1}} \tag{19}$$

During the numerical integration, both V_n^{BT} and V_n^{BC} were interpolated into the time step from the bi-monthly values of the volume transport listed in Table 2.

On the lateral open boundaries temperature (T) and salinity (S) are prescribed at the inflow boundaries, whereas at the outflow boundaries, the advection equation, namely,

$$\frac{\partial}{\partial t}(T,S) + V_n \frac{\partial}{\partial n}(T,S) = 0 \tag{20}$$

is solved for both barotropical and baroclinic modes.

C. STABILITY CONSTRAINTS

The stability constraints were derived from various linearized subsets of equations (Blumberg and Mellor, 1987). Since Δx=*20 km*, H_{max}=*5000 m*, and U_{max} = *1 m/s*, the typical CFL condition derived from Blumberg and Mellor (1987) for the external mode is 45 *s* and for the internal mode is 2000 *s*. In our numerical model, the time step was set as 25 *s* for the external mode and as 900 *s* for the internal mode.

D. SURFACE FORCING

The atmospheric forcing includes wind forcing and thermodynamic forcing. We took the monthly mean climatological wind stress data (Hellerman and Rosenstein, 1983) as the wind data for the middle of the month and interpolated them for each day. The wind stress has a typical magnitude of 1 dyne/cm^2 (corresponding to a surface wind speed

of 10 m/s). Northeasterly winds dominate during the winter and spring seasons while southwesterly winds prevail during the summer monsoon season.

There are two approaches to setting up the surface thermal forcing: (1) flux forcing when the surface heat and salt fluxes, Q_H(W m^{-2}) and Q_S(m s^{-1}) are given, and (2) restoring forcing when the fluxes are not given and the model surface temperature *(T)* and salinity *(S)* are relaxed to the observed values (T_{ob}) and (S_{ob}) :

$$K_H \frac{\partial T}{\partial z} = \alpha_1 Q_H + \alpha_2 C(T_{ob} - T), \tag{21}$$

$$K_H \frac{\partial S}{\partial z} = \alpha_1 Q_S + \alpha_2 C(S_{ob} - S),$$

where K_H is the thermal exchange coefficient and C is the relaxation constant taken to be 0.7 m/d, which is equivalent to a relaxation time of 43 days for an upper layer 30 m thick. (α_1, α_2) are (0,1)-type switcher parameters: when $\alpha_1 = 1, \alpha_2 = 0$, only flux forcing is present; $\alpha_1 = 0, \alpha_2 = 1$, only the restoring forcing is present, $\alpha_1 = 1, \alpha_2 = 1$, both flux forcing and the restoring forcing are present. Process studies usually use only the restoring forcing as the surface thermal forcing (e.g., Brady and Gent, 1994). Therefore, in this simulation we use only the restoring forcing. We construct the (T_{ob}, S_{ob}) data through interpolation from the monthly mean temperature and salinity data (Levitus, 1982). Both the horizontal and vertical resolutions of the Levitus (T,S) data are different from our model resolution. Hence, we use optimal interpolation (OI) to convert the Levitus (T,S) data to our model grids.

E. MODEL SIMULATED SST FIELDS

The model was initiated from April mean (T,S) fields (Levitus, 1982) and forced by the surface wind stress (Hellerman and Rosenstein, 1983) and thermodynamical fluxes depicted in (21). The model was integrated for three years. The third year's outputs were used for discussion.

Three days of the simulated surface currents were picked for investigating the time evolution of the circulation pattern. We choose 30 January for the winter monsoon

forcing, 30 March for the boreal spring forcing, and 30 April for the pre-summer monsoon forcing.

On 30 January a strong southward coastal jet is present near the Vietnam coast, and no cyclonic or anticyclonic rotation is observed in the central SCS (Figure 24a). The isolines of SST in the central SCS are almost parallel to the southeast China coast (Figure 25a).

On 30 March the strength of the southward Vietnam coastal current is greatly reduced. An anticyclone with a strong northward branch is generated between 13°N-18°N, 111°E-115°E (Figure 24b). Several small cyclones are also simulated, e.g., a small and weak one (next to the anticyclone) is located at 13°E-16°E, 115°E-116°E. A warm-core eddy is also simulated associate with the anticyclone (Figure 25b).

On 30 April the southward coastal jet disappears near the Vietnam coast. In the SCS an anticyclone persists between 13°N-18°N, 111°E-115°E (Figure 24c). A warm-core eddy is also simulated associate with the anticyclone (Figure 25c).

The simulations confirm our scenario for the warm-core eddy formation under the climatological forcing. The cold-core eddy formation during El Niño events should be studied in the future research.

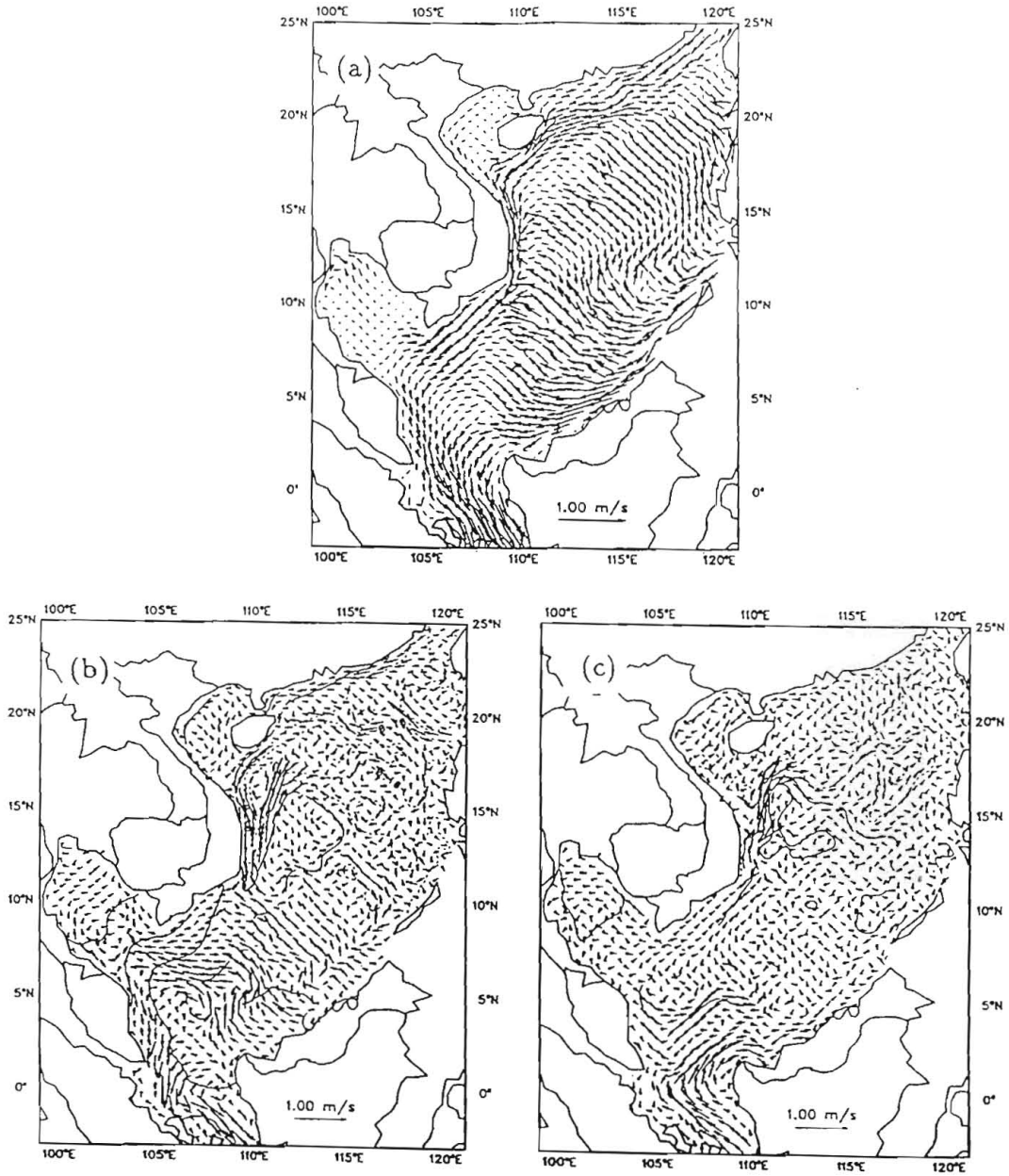

Figure 24. Model Simulation of Surface Circulation for (a) 30 *January*, (b) 30 March, and (c) 30 April.

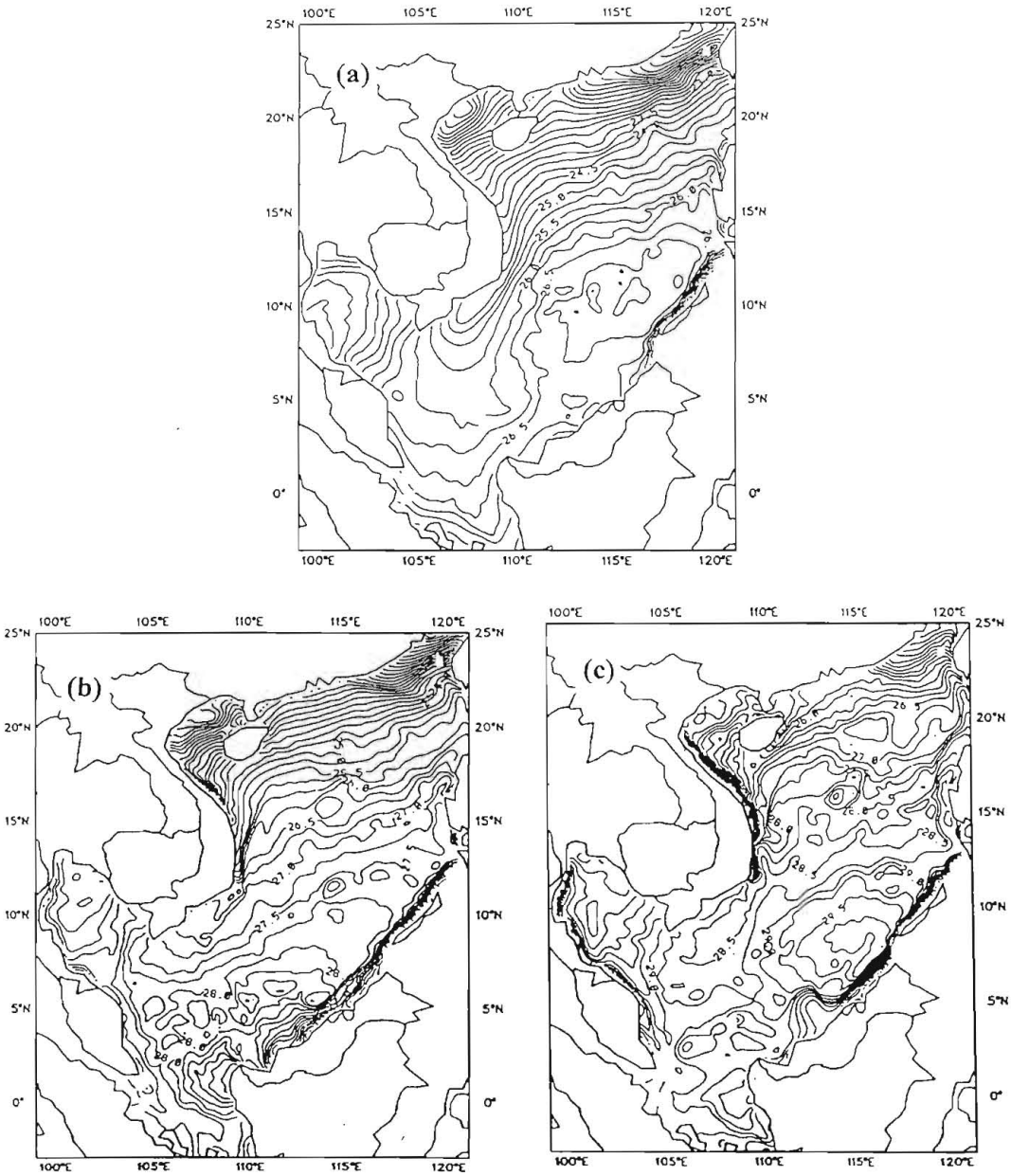

Figure 25. Model Simulation of SST (°C) for (a) 30 January, (b) 30 March, and (c) 30 April.

V. CONCLUSIONS AND RECOMMENDATIONS

A. CONCLUSIONS

The goal of our study was to detect the meso-scale eddies in the central South China Sea during the winter and spring seasons from the Navy's Master Observational Oceanographic Data Set (MOODS), and to investigate mechanisms for the eddy formation. Optimal interpolation, a composite analysis and an EOF analysis were used to study the first objective; a 3-D numerical model was used for the second objective.

After quality control procedures were employed, the data set was composed of 180,059 observed profiles spanning the years 1964 to 1984. Due to a sparsity of data, ten-day bins were constructed for each year. Optimal interpolation (OI) was used to establish a gridded SST data set for the SCS. We applied optimal interpolation to construct a ten-day interval synoptic data set (756 total) from 1-10 January 1964 to 21-31 December 1984 on a 0.5° x 1° grid (finer resolution in the zonal direction) from the MOODS temperature data. The gridded data size is 45x25x756.

The composite analysis on the gridded data set indicates that the annual mean SST seasonal variation has four stages: (1) a cooling phase, (2) an early warming phase, (3) a central SCS warming phase, and (4) a mature warming phase. A warm-core eddy starts to occur in the early warming phase and persists until the end of the central SCS warming phase. It disappears in the mature warming phase.

The EOF analysis of the SST anomaly data shows an eddy in the central SCS being present in the second principal mode. The eddy has distinctive thermal features between non-El Niño and El Niño years. During non-El Niño years the central SCS has a warm-core eddy. However, during El Niño years the central SCS has a cold-core eddy. This implies that the eddy formation in the central SCS is related to the global atmospheric circulation.

A hypothesis for the SCS eddy formation under the climatological forcing (more likely non-El Niño years) was also proposed in this study. During late winter an atmospheric anticyclone over the central SCS generates downwelling and in turn prevents the cold deep water from being advected to the surface. As solar radiation increased in the late winter monsoon, the central SCS surface water is heated more than the surrounding waters by the downwelling effect. This will promote the formation of a warm-core eddy in the central SCS. As the central SCS warm-core eddy persists, being a few degrees warmer than its surroundings, an atmospheric surface low pressure center will be generated above the warm water, which may trigger the summer monsoon onset. After the summer monsoon onset, an atmospheric surface cyclone occupies the central SCS. This cyclone will generate upwelling in the central SCS, which advects the deep cold water into the surface mixed layer. This upwelling effect will finally destroy the central SCS warm-core eddy. This downwelling hypothesis on the SCS warm-core eddy formation during non-El Niño years was verified by a 3-D primitive equation model. The air-sea feedback scenario has not been verified for El Niño events.

B. RECOMMENDATIONS

We recommend that further studies should incorporate (1) 3-D thermal features of the SCS meso-scale eddies, (2) constructing a composite for the SCS surface wind fields, to test if they are upwelling or downwelling favorable wind field; (3) running the 3-D numerical model under the El Niño wind forcing.

APPENDIX A. TIME SERIES OF EOF 3 AMPLITUDES FOR 1967-84

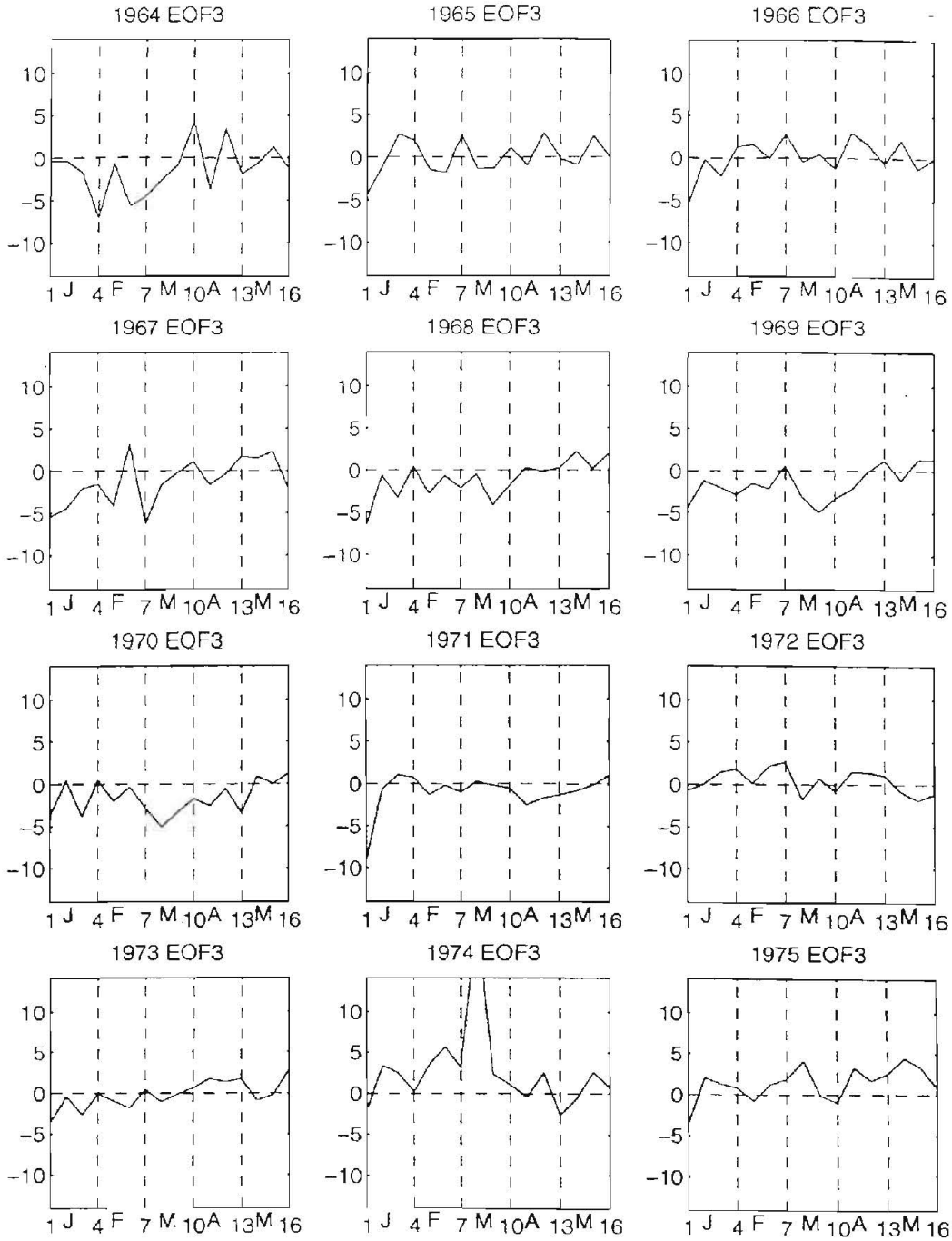

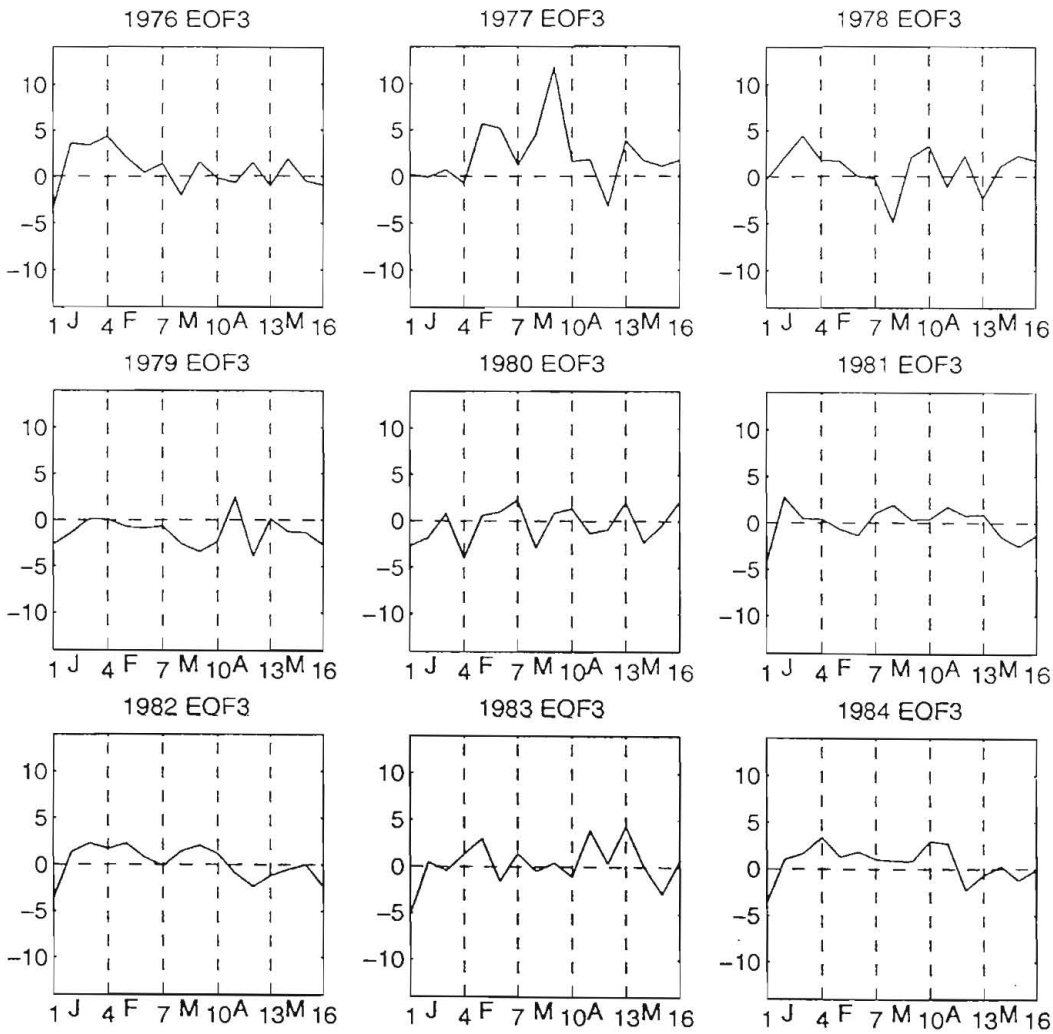
1976 EOF3
1977 EOF3
1978 EOF3
1979 EOF3
1980 EOF3
1981 EOF3
1982 EOF3
1983 EOF3
1984 EOF3
10
5
0
−5
−10
1 J 4 F 7 M 10A 13M 16

APPENDIX B. TIME SERIES OF EOF 4 AMPLITUDES FOR 1967-84

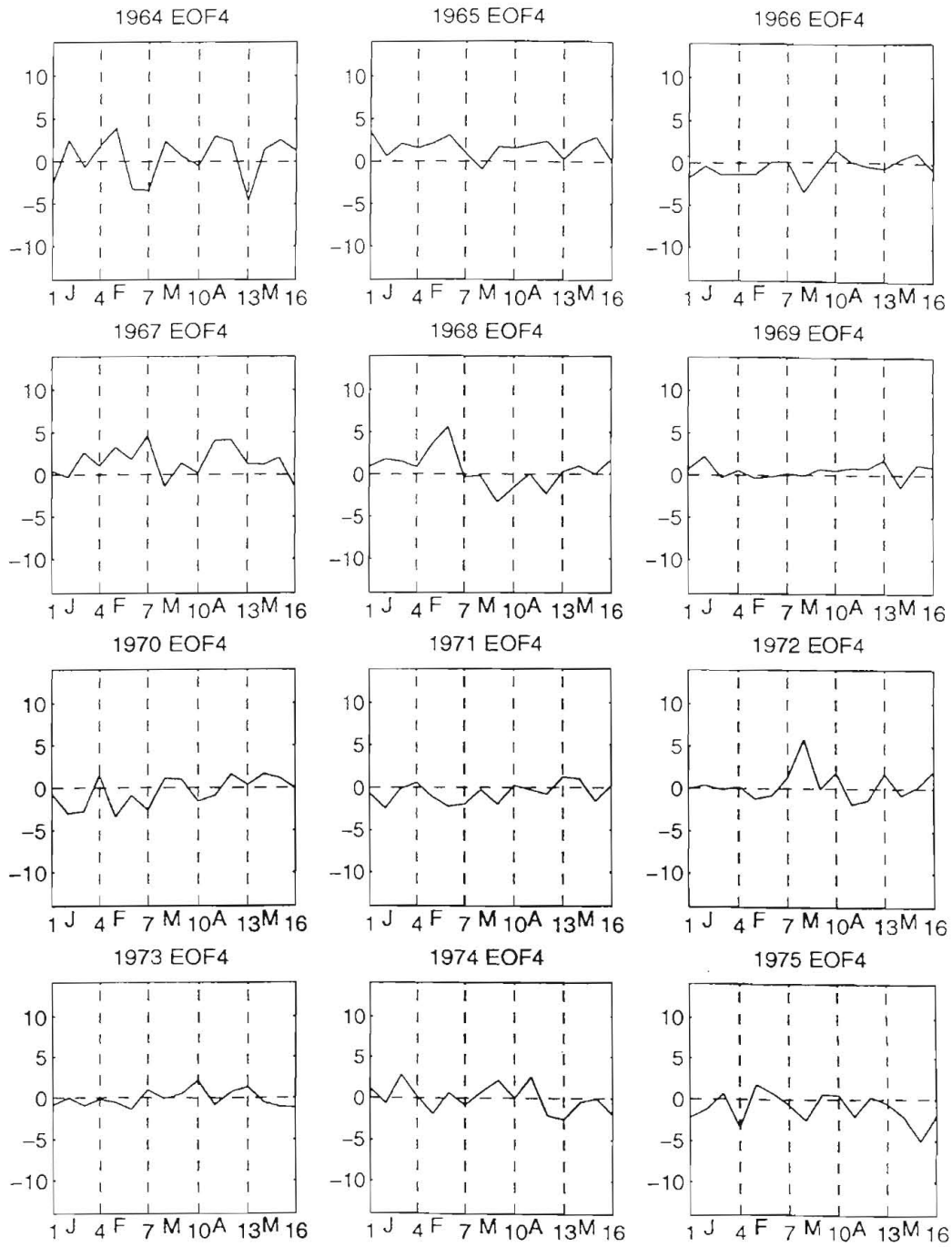

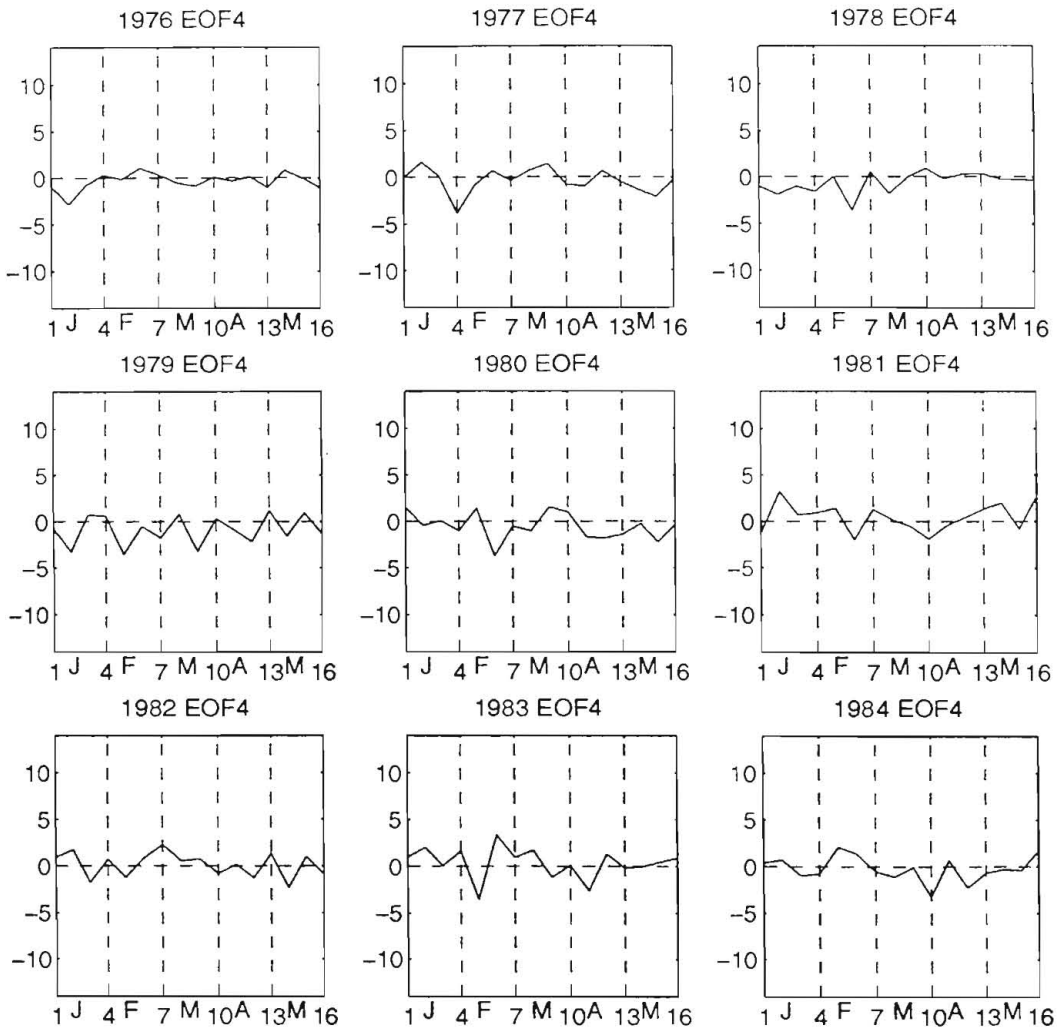
1976 EOF4
1977 EOF4
1978 EOF4
1979 EOF4
1980 EOF4
1981 EOF4
1982 EOF4
1983 EOF4
1984 EOF4
10
5
0
−5
−10
1 J 4 F 7 M 10A 13M 16

APPENDIX C. TIME SERIES OF EOF 5 AMPLITUDES FOR 1967-84

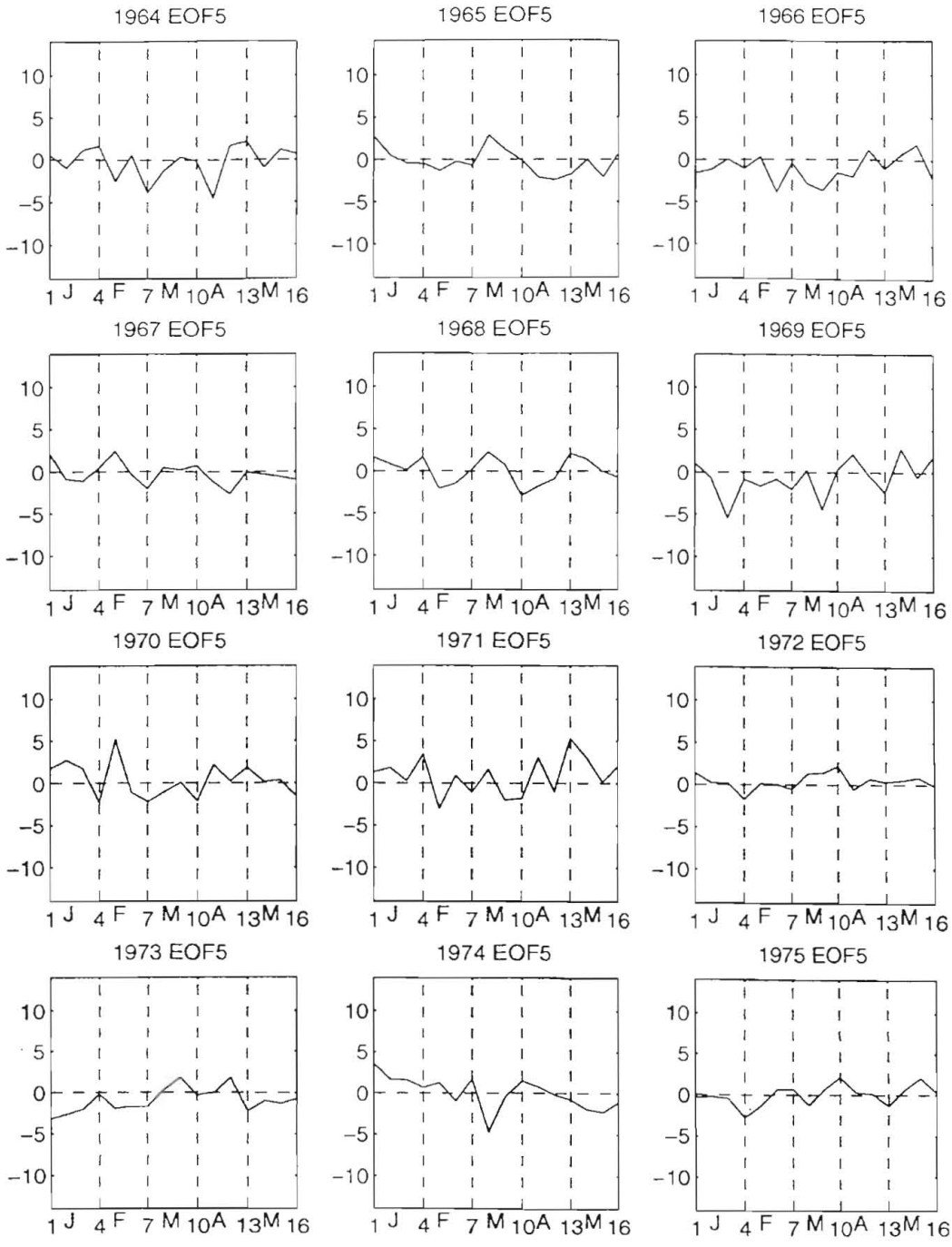

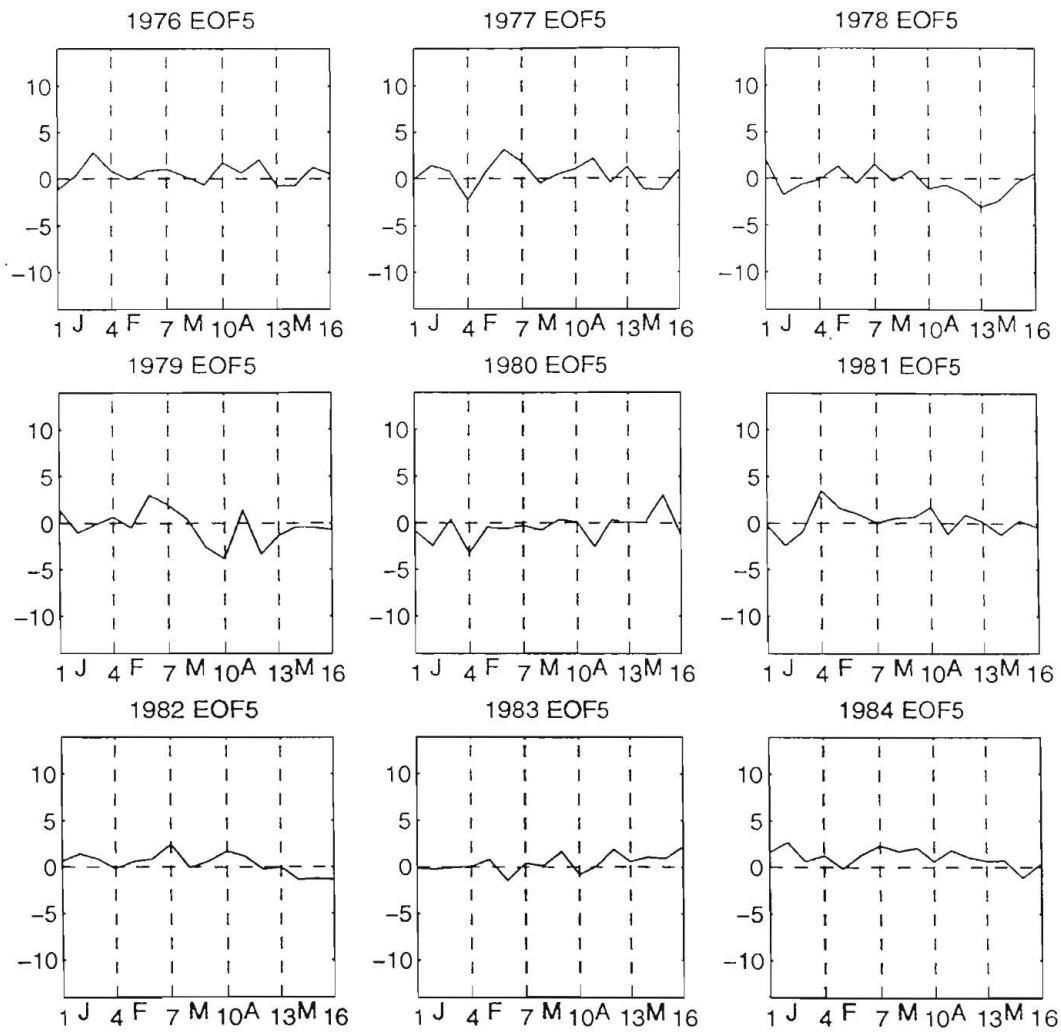
1976 EOF5
1977 EOF5
1978 EOF5
1979 EOF5
1980 EOF5
1981 EOF5
1982 EOF5
1983 EOF5
1984 EOF5
10
5
0
−5
−10
1 J 4 F 7 M 10A 13M 16

APPENDIX D. TIME SERIES OF EOF 3 AMPLITUDES AVERAGE ANOMALY

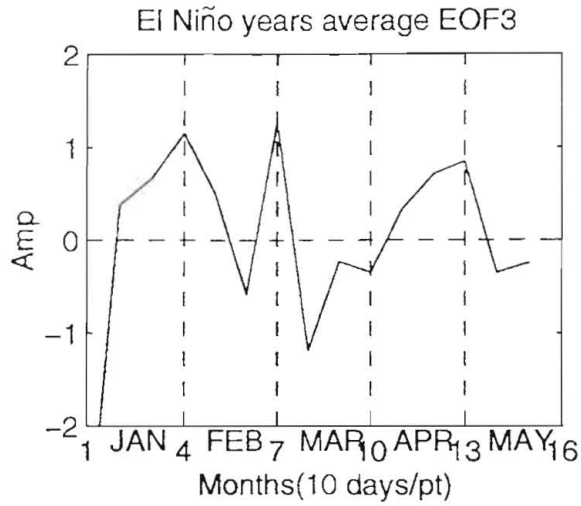

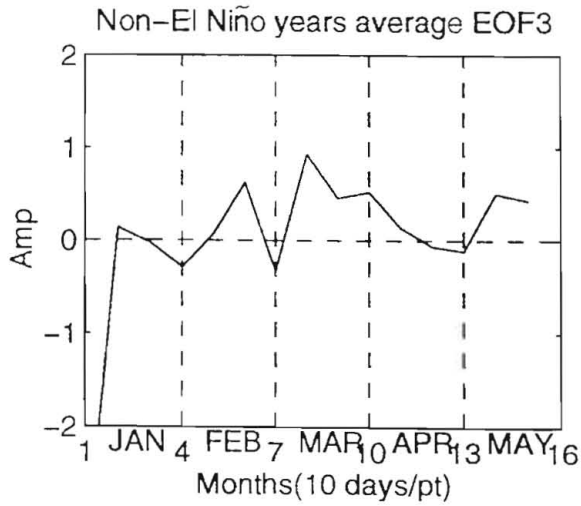

APPENDIX E. TIME SERIES OF EOF 4 AMPLITUDES AVERAGE ANOMALY

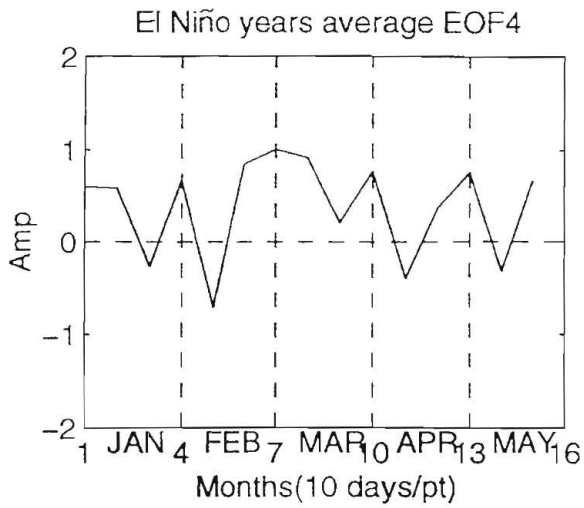

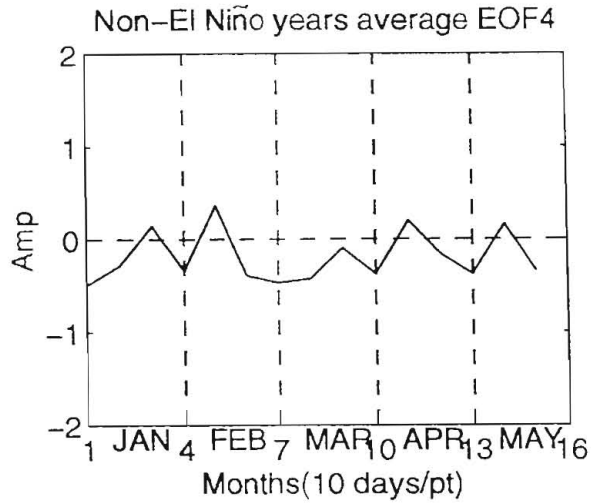

APPENDIX F. TIME SERIES OF EOF 5 AMPLITUDES AVERAGE ANOMALY

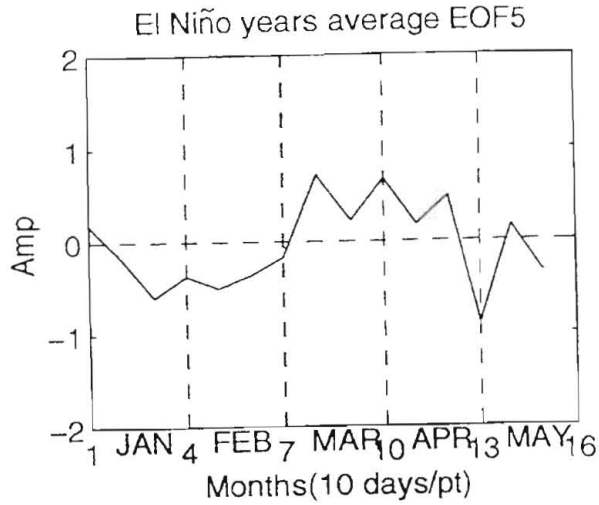

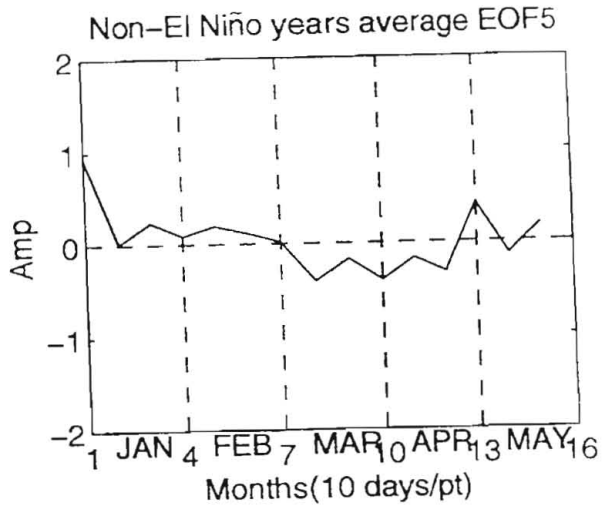

LIST OF REFERENCES

Arakawa, A., and V. R. Lamb, 1977: "Computational Design Of The Basic Dynamical Processes Of The UCLA General Circulation Model." *Methods in Computational Physics*, 17, Academic Press, New York, 119-143.

Blumberg, A.F., and G.L. Mellor, 1978: "A Description Of A Three-Dimensional Coastal Ocean Circulation Model." In: *Three Dimensional Coastal Ocean Models* (Edited by N.S. Heaps), American Geophysical Union, 1-16.

Brady, E. C., and P. R. Gent, 1994: "The Seasonal Cycle of Meridional Heat Transport in a Numerical Model of Pacific Equation Upwelling Zone.", *Journal of Physical Oceanography*, 24, 2658-2673.

Bryan, K., 1969: "A Numerical Method For The Study Of The Circulation Of The World Ocean." *Journal of Computational Physics*, 4 (3), 347-376.

Cheang, B.K., 1980: "Some Aspects Of Winter Monsoon And Its Characteristics In Malaysia." Research Publication No. 2, Malaysian Meteorological Service.

Chu, P.C., C.C. Li, D.S. Ko, and C.N.K. Mooers, 1994: "Response Of The South China Sea To Seasonal Monsoon Forcing." Proceedings, Second International Conference on Air-Sea Interaction and Meteorology and Oceanography of the Coastal Zone, 22-27 September 1994, Lisbon Portugal 214-215.

Chu, P.C., 1995: "Monsoon Effects On The South China Sea Circulation." Abstract, the 21st International Association for the Physical Sciences of the Oceans, Hawaii, 74.

Chu, P.C., and C.P. Chang (1995a) "A Case Study Of The South China Sea Warm Pool." The International CLIVAR-GOALS Workshop on Asian-Australian Monsoon Oceanography and Meteorology, April 10-12, Melbourne, Australia.

Chu, P.C., and C.P. Chang (1995b) "South China Sea Warm Pool And Monsoon Development." The International South China Sea Monsoon Experiment (SCSMEX) Scientific Workshop, June 5-7, Beijing, China.

Clancy, R.M., P.A. Phoebus, and K.D. Pollak, 1990: "An Operational Global Scale Ocean Thermal Analysis System." *Journal of Atmospheric and Oceanic Technology*, 7, 233-254.

Dale, W.L., 1959: "Winds And Drift Currents In The South China Sea." *Malayan Journal of Tropical Geography,* 8, 1-31.

Fofonoff, N.P., 1962: Physical Properties of Sea-water. In: The Sea, Vol. 1 (edited by N.M. Hill), Intersciences, New York, 347-376.

Gandin, L.S., (1965) "Objective Analysis Of Meteorological Fields." *Israel Program for Scientific Translation*, pp. 242.

Hellerman, S., and M. Rosenstein, 1983: "Normal Monthly Wind Stress Over The World Ocean With Error Estimates." *Journal of Physical Oceanography*, 13, 1093-1104.

Huang, Q.Z., W.Z. Wang, Y.S. Li, and C.W. Li, 1994: Current Characteristics Of The South China Sea. In: *Oceanology of China Seas* (Edited by D. Zhou, Y.B. Liang, and C.K. Tseng). Kluwer Academic Publishers, Boston.

Kuo, H.L., 1989: "Long-Term Oscillation in the Coupled Atmosphere-Ocean An El Niño Phenomenon." *Journal of Climate*, 2, 1421-1437.

Levitus, S., 1984: Climatological Atlas Of The World Ocean. NOAA Professional Paper, 13, U.S. Government Printing Office, Washington, D.C.

Mellor, G.L., and T. Yamada, 1974: "A Hierarchy Of Turbulence Closure Models For Planetary Boundary Layer." *Journal of Atmospheric Sciences*, 31, 1791-1796.

Mellor, G.L., and T. Yamada, 1982: Development Of A Turbulence Closure Model For Geophysical Fluid Problems. *Reviews of Geophysics and Space Physics*, 20, 851-875.

Nitain, H., 1970: "Oceanographic Conditions In The Sea East Of Philippines And Luzon Strait In Summer Of 1965 And 1966." In: *The Kuroshio-A Symposium on Japan Current* (J.D. Marr edited), East-West Press, Honolulu, 213-232.

Smagorinsky, J., 1963: "General Circulation Experiments With The Primitive Equations." *Monthly Weather Reviews*, 91, 99-164.

Soong, Y.S., J.H. Hu, C.R. Ho, and P.P. Niiler, 1995: "Cold-Core Eddy Detected In South China Sea." EOS, Volume 76, 345-347.

Sprintall, J., and G. Meyers (1991) "An Optimal XBT Sampling Network For The Eastern Pacific Ocean." *Journal of Geophysical Research*, 96, 10539-10552.

Uda, M., and T. Nakao, 1972: "Water Masses And Currents In The South China Sea And Their Seasonal Changes." In: *The Kuroshio-Proceedings of the 3rd CSK Symposium*, Bangkok, Thailand, 161-188.

White, W.B., and R.L. Bernstein, 1979: "Design Of An Oceanographic Network In The Mid-Latitude North Pacific." *Journal of Physical Oceanography*, 9, 592-606.

White, W.B., G. Meyers, and K. Hasunuma (1982) "Space/Time Statistics Of Short-Term Climatic Variability In The Western North Pacific." *Journal of Geophysical Research*, 87, 1979-1989.

Wyrtki, K., 1961: "Scientific Results Of Marine Investigations Of The South China Sea And Gulf Of Thailand 1959-1961." NAGA Report, 2, The University of California Scripps Institution of Oceanography, La Jolla, California.

INITIAL DISTRIBUTION

		No. Copies
1.	Defense Technical Information Center Cameron Station Alexandria, VA 22304-6145	2
2.	Library, Code 52 Naval Postgraduate School Monterey, CA 93943-5101	2
3.	Chairman (Code OC/BF) Department of Oceanography Naval Postgraduate School Monterey, CA 93943-5002	1
4.	Chairman (Code MR/HY) Department of Meteorology Naval Postgraduate School Monterey, CA 93943-5002	1
5.	Professor Peter C. Chu (Code OC/CU) Department of Oceanography Naval Postgraduate School Monterey, CA 93943-5002	3
6.	Professor Chih-Pei Chang (Code MR/CP) Department of Meteorology Naval Postgraduate School Monterey, CA 93943-5002	1
7.	Ms. Bao Fong Jeng (Code MR/JG) Department of Meteorology Naval Postgraduate School Monterey, CA 93943-5002	1
8.	Lieutenant Charles R. Fralick, Jr. 3824 Larchwood Dr. Virginia Beach, VA 23456	1

9.	Lieutenant Huang, Ming-Jer NPGS SGC 1136 Monterey, CA 93943-5002	1
10.	Lieutenant Commander Tseng, Hsing-Chia No. 415, Hwa Jung Rd., Ku Shan District, Kaohsiung, Taiwan, R.O.C.	3
11.	Department of Oceanography National Taiwan University 1 Roosevelt Road, Sec. 4 Taipei, Taiwan, R.O.C.	1
12.	Chinese Naval Academy Library P.O. Box 90175 Tsoying, Kaohsiung, Taiwan, R.O.C.	1
13.	Department of Oceanography National Chung Shan University Ku Shan District, Kaohsing, Taiwan, R.O.C.	1